Supporting Information

Double-spiroring-structured Mechanophore with Dual-signal Mechanochromism and Multistate Mechanochemical Behavior: Non-sequential Ring-opening and Multimodal Analysis

Huan Hu,[a] Xin Cheng,[a] Zhimin Ma,[b] Zhijian Wang[c] and Zhiyong Ma[a,d]*

[a]   Prof. Z.Y. Ma, Mr. H. Hu, Mr. X. Cheng
Beijing Advanced Innovation Center for Soft Matter Science and Engineering, State Key Laboratory of Organic-Inorganic Composites, College of Chemical Engineering, Beijing University of Chemical Technology, Beijing 100029, China. E-mail: mazhy@mail.buct.edu.cn.

[b]   Dr. Z.M. Ma
College of Engineering, Peking University, Beijing 100871, China.

[c]   Prof. Z.J. Wang
Key Laboratory of Aerospace Advanced Materials and Performance, Ministry of Education, School of Materials Science and Engineering, Beihang University, Beijing 100191, China.

[d]   Prof. Z.Y. Ma
State Key Laboratory of Molecular Engineering of Polymers, Fudan University, Shanghai 200438, China.

Table of Contents

I. Materials and General Methods

All the solvents and reactants were purchased from commercialized companies and used as received without further purification except for specifying otherwise. Methyl acrylate was passed through a short column of basic alumina to remove inhibitor immediately prior to use. THF was dried with 3A molecular sieves or purchased to obtain anhydrous THF.

^{1}H NMR and ^{13}C NMR spectra were recorded on the 400 MHz Bruker Avance III HD nuclear magnetic resonance spectrometer at room temperature with CDCl$_3$ as the solvent and tetramethylsilane (TMS) as the internal standard. High resolution mass spectra (HRMS) were obtained from a Bruker Solarix XR time-of-flight mass spectrometer (ESI+).

Fluorescence spectra were recorded at room temperature on the Hitachi F-4600 FL Spectrophotometer (365nm excitation). UV-vis absorption spectra were recorded on Hitachi U-3900H Spectrophotometer, WI lamp (Visible light region) switched to D2 lamp (Ultraviolet region) at 340 nm during scanning.

Analytical gel permeation chromatography (GPC) was performed on a Waters 1525 Gel chromatography with three mixed-bed GPC columns in series (three Waters Styragel HT3 THF (7.8*300mm Column)), and THF mobile phase run at 35 °C and a flow rate of 1 mL/min for 40 min. The differential refractive index of poly(methyl acrylate) was monitored using a WAT038040 (2414) detector.

Ultrasound experiments were performed on Lawson Scientific DH92-IIN ultrasonic generator equipped with a 10 mm diameter solid probe / horn. The poly(methyl acrylate) (~150mg) was dissolved in ~15 mL anhydrous THF. The sonication power was set at 60% amplitude (rated power: 650W and the actual input power is calibrated to be 12.12 W/cm^{-2}) with 1 s on and 1 s off. The solution is sonicated in a glass vessel immersed in an ice bath (0 °C) or an ethyl acetate bath, which liquid nitrogen is poured into before sonication. The bath maintains a liquid-solid state during sonication, and the temperature is estimated to be the freezing point of ethyl acetate, -84 ℃.

II. Synthetic Procedures
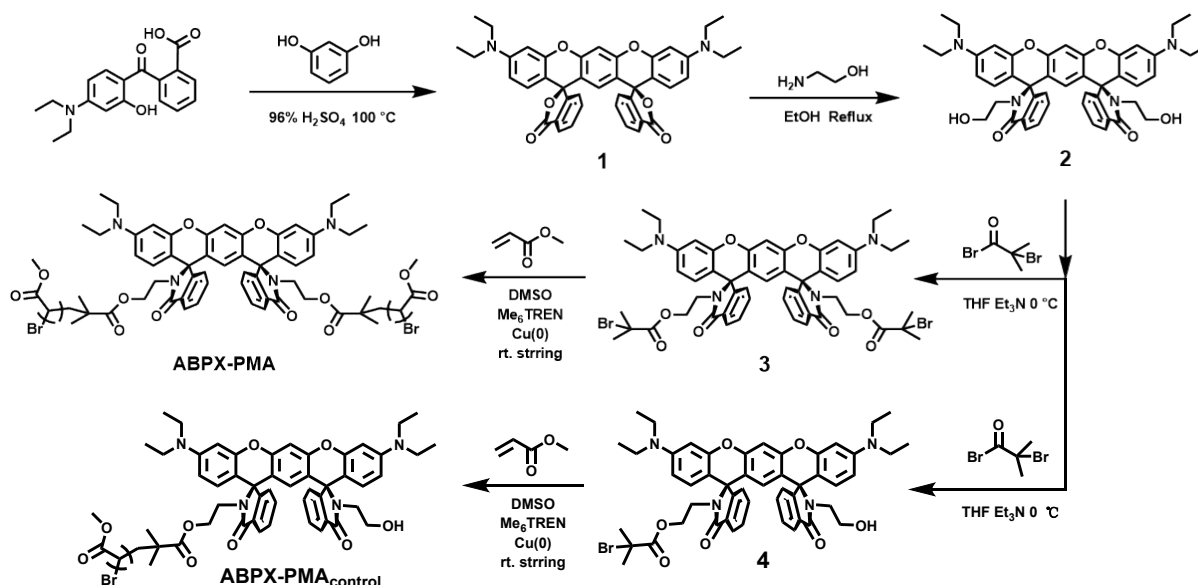
Scheme S1. Synthesis of ABPX initiators and ABPX-PMA.

Compound 1: 2-(4-(diethylamino)-2-hydroxybenzoyl)benzoic acid (2.5 g, 8 mmol) and resorcinol (0.44g, 4 mmol) were both placed in 150 ml round-bottomed flask. Concentrated sulfuric acid (10 ml) was then added and the solution was kept stirring at 100 °C for 6 h. After the mixture was cooled down to room temperature and poured into ice water (100 mL). The mixture was neutralized with sodium hydroxide (15 g) and then extracted with dichloromethane (50 mL) three times. The organic layers were dried over anhydrous sodium sulfate and evaporated to give the crude product of the mixture of *cis*-ABPX and *trans*-ABPX. The purification and separation of the stereoisomer were achieved by silica column chromatography eluting with dichloromethane and ethanol (100:1) to give the pure form of *cis*-ABPX (1) as a pink solid. Yield: 30%.

<u>^{1}H NMR (400 MHz, Chloroform-*d*)</u> δ: 7.84 – 7.79 (m, 2H), 7.45 – 7.39 (m, 4H), 7.13 (s, 1H), 6.94 – 6.89 (m, 2H), 6.51 – 6.44 (m, 4H), 6.32 (dd, *J* = 9.1, 2.6 Hz, 2H), 5.98 (s, 1H), 3.36 (q, *J* = 7.1 Hz, 8H), 1.17 (t, *J* = 7.0 Hz, 12H).

¹³C NMR (101 MHz, Chloroform-*d*) δ: 168.93, 153.36, 153.22, 152.23, 149.80, 134.20, 129.36, 128.76, 128.60, 127.38, 124.97, 123.53, 116.44, 108.65, 105.31, 104.39, 97.93, 83.34, 44.66, 12.60.

Compound 2: A round bottom flask equipped with a stir bar was charged with compound 1 (0.30 g, 0.45 mmol) and ethanolamine (0.82 g 13.4 mmol) dissolved in ethanol (20 mL). The solution was heated to reflux in an oil bath (80 °C-90 °C) for 24 h. The reaction mixture was cooled to room temperature and then concentrated under reduced pressure to remove ethanol. The residue was dissolved in 50 mL dichloromethane and washed with saturated saline (30 mL) three times to remove unreacted ethanolamine. The organic layers were dried over anhydrous sodium sulfate and evaporated. The crude product was purified by column chromatography on silica gel (2~5 % ethanol/dichloromethane) to give a reddish white powder. Yield: 20 %.

¹H NMR (400 MHz, Chloroform-*d*) δ: 7.85 – 7.79 (m, 2H), 7.45 (dd, *J* = 5.7, 3.1 Hz, 4H), 7.03 (s, 1H), 6.98 – 6.91 (m, 2H), 6.46 – 6.40 (m, 4H), 6.31 (dd, *J* = 8.9, 2.6 Hz, 2H), 6.08 (s, 1H), 3.35 (q, *J* = 7.1 Hz, 8H), 3.26 – 3.13 (m, 4H), 2.97 – 2.86 (m, 4H), 1.18 (t, *J* = 7.0 Hz, 12H).

¹³C NMR (101 MHz, Chloroform-*d*) δ: 169.80, 153.24, 152.60, 152.54, 149.06, 133.00, 129.38, 128.79, 128.21, 127.68, 123.43, 122.98, 115.76, 108.87, 104.40, 103.79, 97.81, 65.00, 61.79, 44.50, 44.40, 12.55.

Compound 3&4: A round bottom flask equipped with a stir bar was charged with compound 2 (0.16 g, 0.213 mmol) and triethylamine (86.3 mg 0.853 mmol) dissolved in 7 mL anhydrous THF. The solution was cooled to 0 °C in an ice bath for 20 min, followed by the consecutive dropwise addition of α-bromoisobutyryl bromide (124.9 mg, 0.543 mmol), resulting in formation of a white precipitate. The reaction mixture was allowed to warm to room temperature and stirred for 24 h. The reaction mixture was filtered to remove ammonium salts

and concentrated under reduced pressure. The crude product was purified by column chromatography on silica gel to give white powder (5~20 % ethyl acetate/petroleum ether for compound 3, yield: 72 %; 1~2 % ethyl acetate/petroleum ether for compound 4, yield: 11 %).

Compound 3

<u>^{1}H NMR (400 MHz, Chloroform-d)</u> δ: 7.82 – 7.76 (m, 2H), 7.44 – 7.37 (m, 4H), 7.06 (s, 1H), 7.01 – 6.94 (m, 2H), 6.41 (d, J = 2.5 Hz, 2H), 6.35 (d, J = 8.9 Hz, 2H), 6.26 (dd, J = 9.0, 2.6 Hz, 2H), 6.05 (s, 1H), 3.48 – 3.24 (m, 14H), 3.04 (ddd, J = 12.8, 7.8, 6.0 Hz, 2H), 1.82 (d, J = 16.2 Hz, 12H), 1.16 (t, J = 7.0 Hz, 12H).

<u>^{13}C NMR (101 MHz, Chloroform-d)</u> δ: 170.86, 168.25, 153.14, 152.58, 152.54, 149.03, 133.16, 129.25, 128.76, 128.29, 128.07, 123.31, 115.94, 108.87, 104.66, 104.11, 97.79, 64.05, 62.44, 55.98, 44.39, 38.00, 30.73, 30.57, 12.56.

<u>HRMS (ESI, m/z):</u> Calcd for $C_{54}H_{57}{}^{79}Br_2N_4O_8$ (M+H)$^+$: 1047.253766. Found: 1047.253436; Calcd for $C_{54}H_{60}{}^{79}Br_2N_5O_8$ (M+NH$_4$)$^+$: 1064.280315. Found: 1064.280095.

Compound 4

<u>^{1}H NMR (400 MHz, DMSO-d_6)</u> δ: 7.58 (dd, J = 12.1, 7.2 Hz, 2H), 7.38 – 7.24 (m, 4H), 7.18 (s, 1H), 6.79 (dd, J = 15.3, 7.4 Hz, 2H), 6.46 – 6.23 (m, 6H), 5.69 (s, 1H), 4.53 (s, 1H), 3.70 (dd, J = 10.0, 5.5 Hz, 1H), 3.54 – 3.43 (m, 2H), 3.32 (d, J = 7.7 Hz, 8H), 3.01 (dt, J = 12.9, 4.8 Hz, 2H), 2.90 (ddd, J = 16.0, 8.9, 3.6 Hz, 3H), 1.80 (d, J = 2.3 Hz, 6H), 1.07 (td, J = 7.0, 2.0 Hz, 12H).

<u>^{13}C NMR (101 MHz, Chloroform-d)</u> δ: 170.72, 167.12, 152.88, 152.81, 152.70, 152.49, 149.20, 149.12, 133.25, 132.99, 130.13, 129.71, 128.93, 128.88, 128.79, 128.14, 123.63, 123.59, 122.63, 122.52, 116.09, 109.39, 109.29, 104.11, 97.60, 63.69, 62.81, 58.61, 57.61, 44.16, 30.52, 30.49, 12.82, 12.77.

<u>HRMS (ESI, m/z):</u> Calcd for $C_{50}H_{51}{}^{79}BrN_4O_7$ (M+H)$^+$: 889.3019. Found: 889.3036.

General Procedure for the Synthesis of Polymers Incorporating a ABPX Mechanophore (ABPX-PMA): A representative procedure is provided for the synthesis of **ABPX-PMA$_{176}$**. A 25 mL Schlenk tube equipped with a stir bar was charged with initiator 3 (9.9 mg, 0.00947 mmol), dry DMSO (2.00 mL), methyl acrylate (2.00 mL, 22.2 mmol) and freshly cut two pieces of copper sheet. The tube was sealed, the solution was degassed via three freeze-pump-thaw cycles, and then the tube was opened and Me$_6$TREN (10 μL, 0.0379 mmol) was added quickly *via* syringe. The tube was sealed again and degassed via another freeze-pump-thaw cycle, and then backfilled with nitrogen and warmed to room temperature. After stirring at room temperature for 3 h, the flask was opened to air and the solution was diluted with DCM (10 mL). The polymer solution was precipitated into cooled methanol (500 mL) three times and the isolated product was dried under vacuum (60 °C) to provide 1.49 g of polymer (78.7 %). M$_n$ = 176.2 kg/mol, Đ = 1.29.

Confirmation of the *cis/trans* configuration of the molecules 2, 3 and ABPX-PMA. We observed a mixture of *cis* and *trans* isomers when compound **1** was converted to compound **2**, even the raw material *cis* **1** was partly isomerized to *trans* form (Figure S1a) due to the harsh reaction condition. The ^{1}H NMR spectra of *cis* and *trans* forms of **2** obtained by silica column chromatography were then compared with the ^{1}H NMR spectra of ABPX-hydrazide reported by Enomoto *et al.*,[1] in which the configurations of ABPX are unequivocally confirmed using single crystals. The similar chemical shifts and splitting types confirm that the compound **2** is *trans* form. For the reaction from **2** to **3**, only one isomer is observed (Figure S1a) and also confirmed to be *trans* form according to the ^{1}H NMR spectra (Figure S1b). Also, isomerization is unlikely to occur in these mild reaction conditions (0 ℃ to rt.). For the synthesis of PMA from **3**, the conditions of reaction and postprocessing are both moderate. Similar aromatic proton signals also confirm that ABPX is *trans* form in PMA, as shown in Figure S1b.
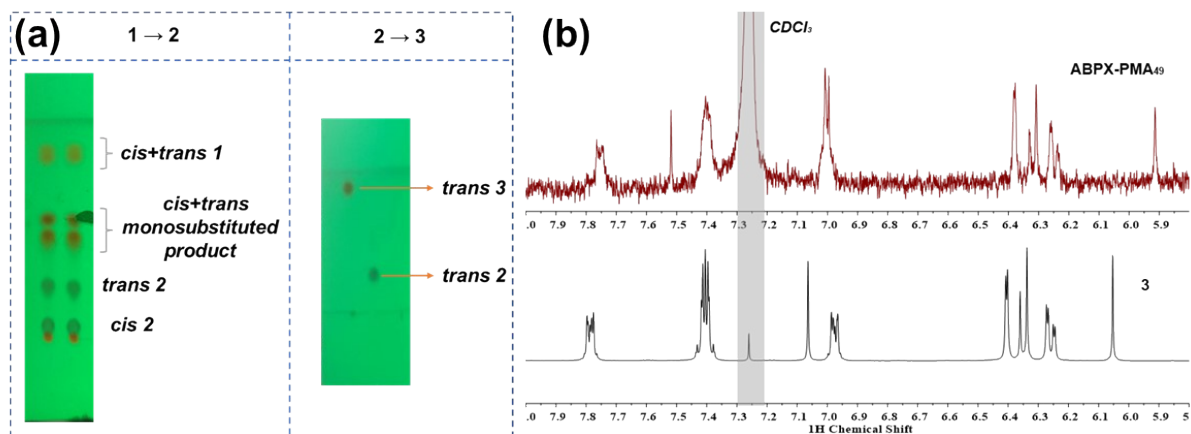
Figure S1. (a) Thin layer chromatography of reactions from compound **1** to compound **2** and from compound **2** to compound **3**. (b) ^{1}H NMR spectra of compound **3** (*trans*) and ABPX-PMA$_{49}$. All ^{1}H NMR spectra display from 5.8 ppm to 8.0 ppm.
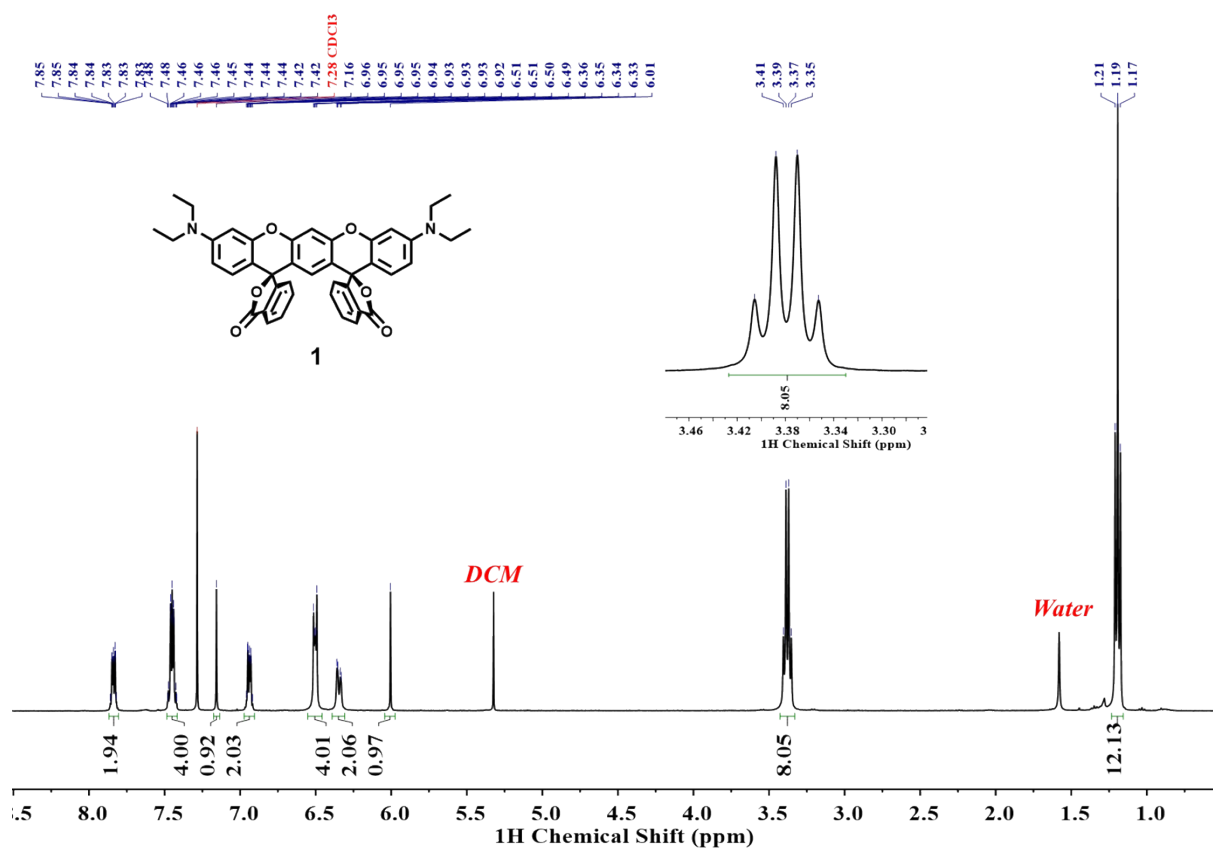
III. Characterize Spectra

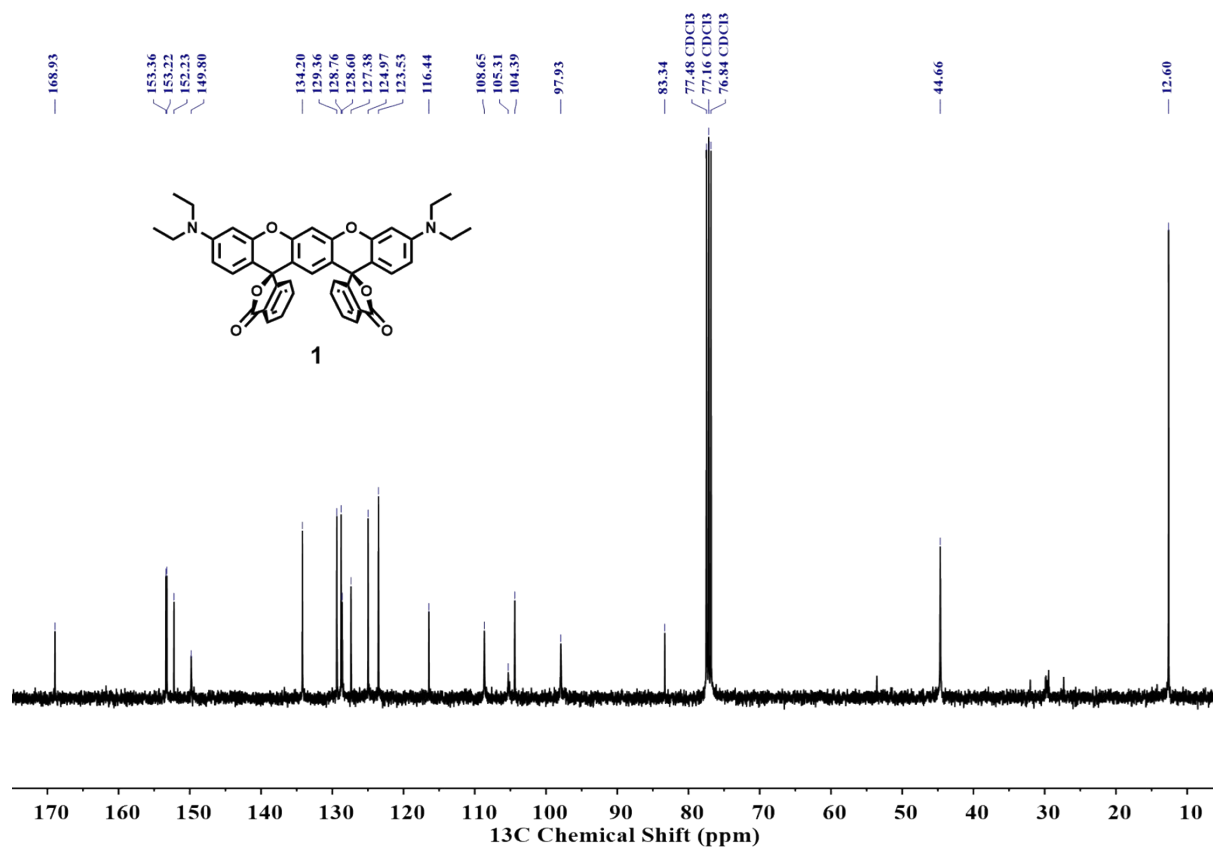Figure S2. ^{1}H NMR spectrum of compound **1** in CDCl$_3$.

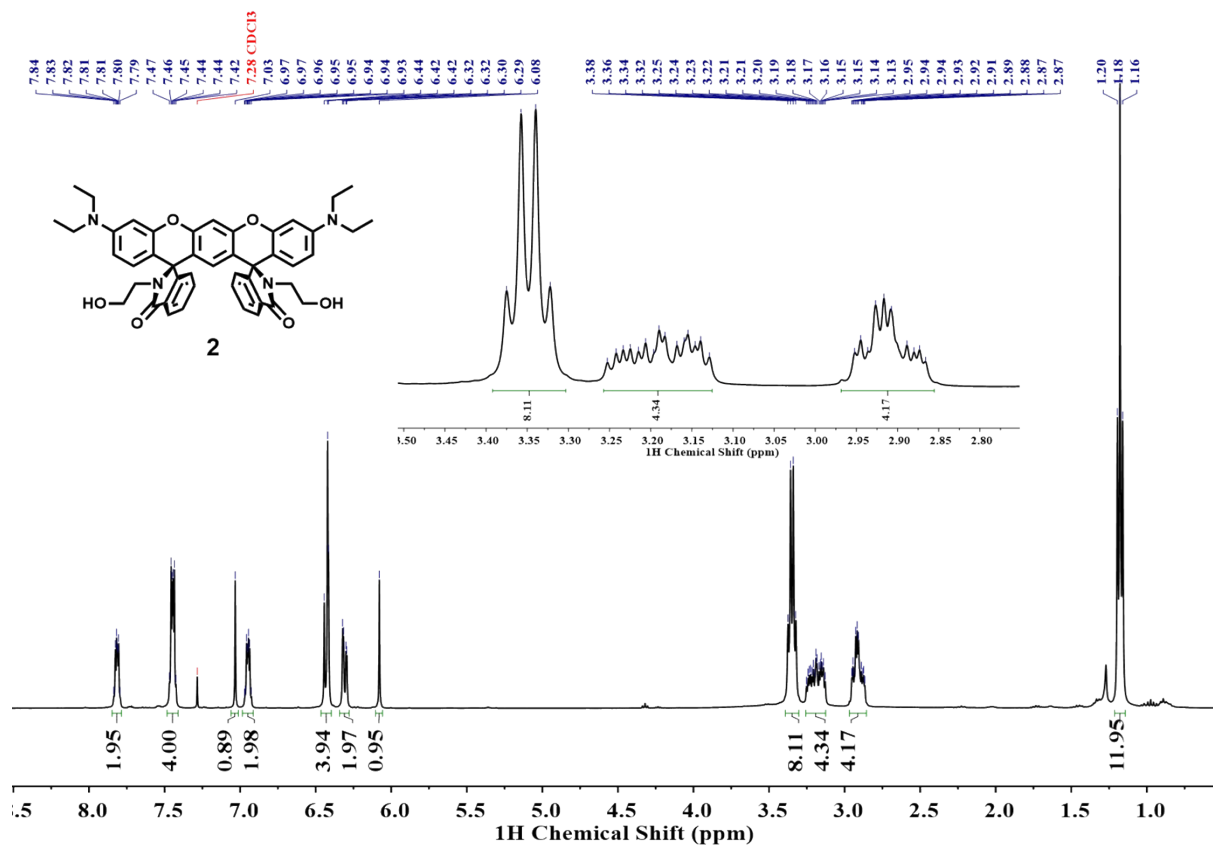Figure S3. ^{13}C NMR spectrum of compound **1** in CDCl$_3$.
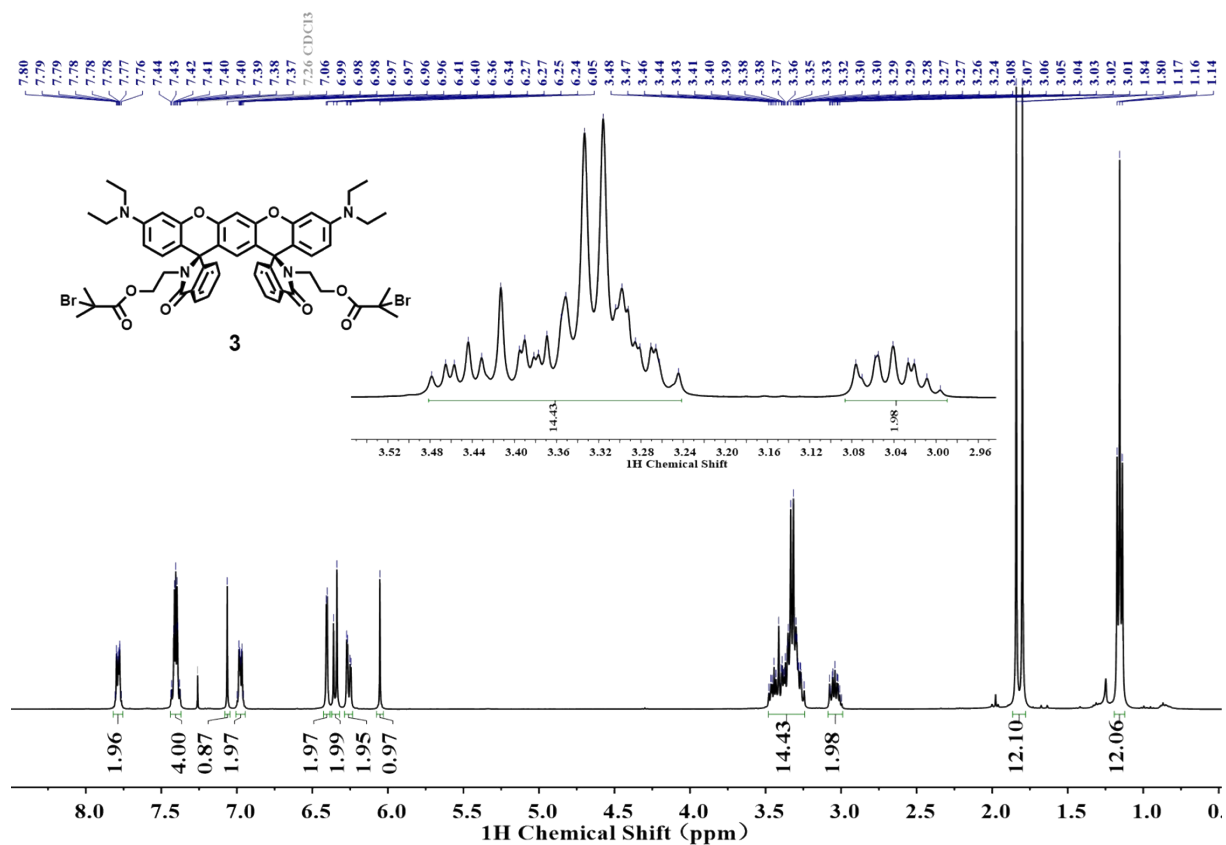
Figure S4. ^{1}H NMR spectrum of compound **2** in CDCl$_3$.
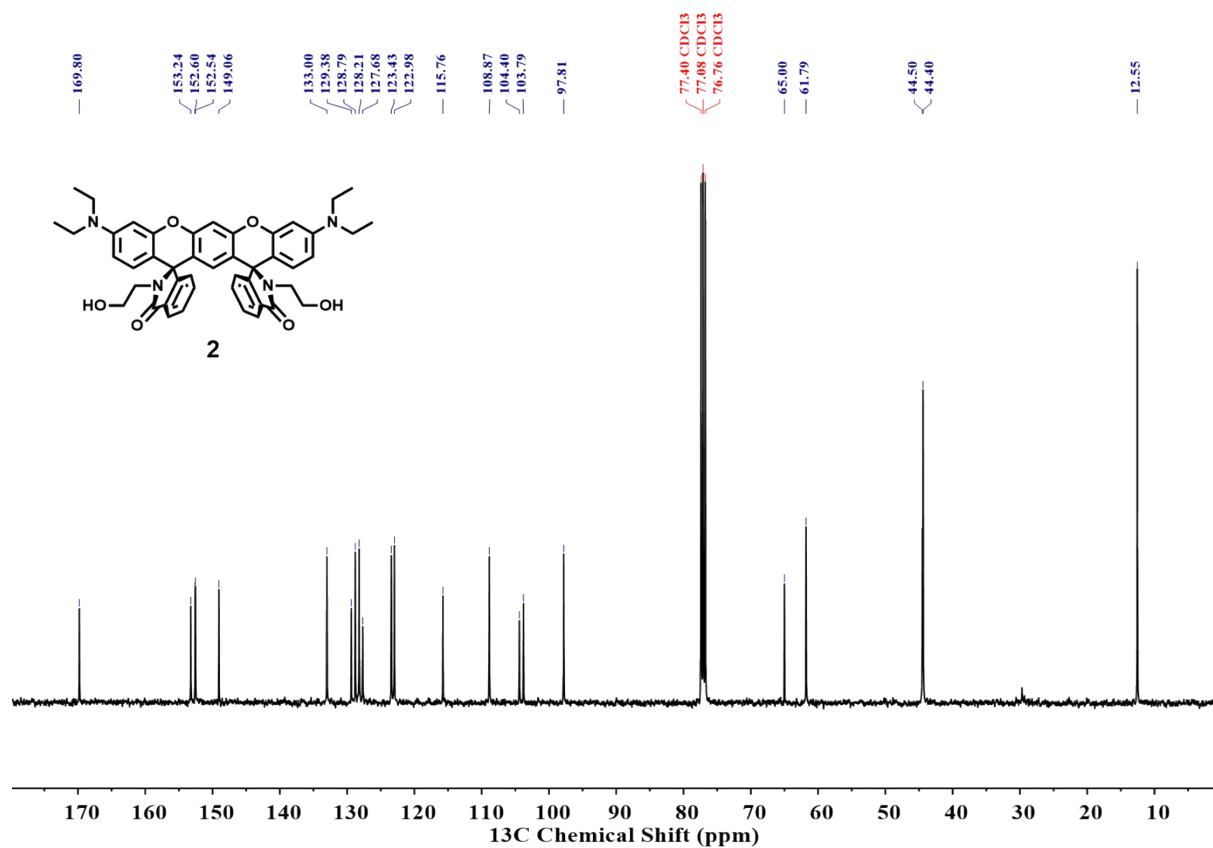
Figure S5. ^{13}C NMR spectrum of dyad **2** in CDCl$_3$.

Figure S6. ^{1}H NMR spectrum of compound **3** in CDCl$_3$.
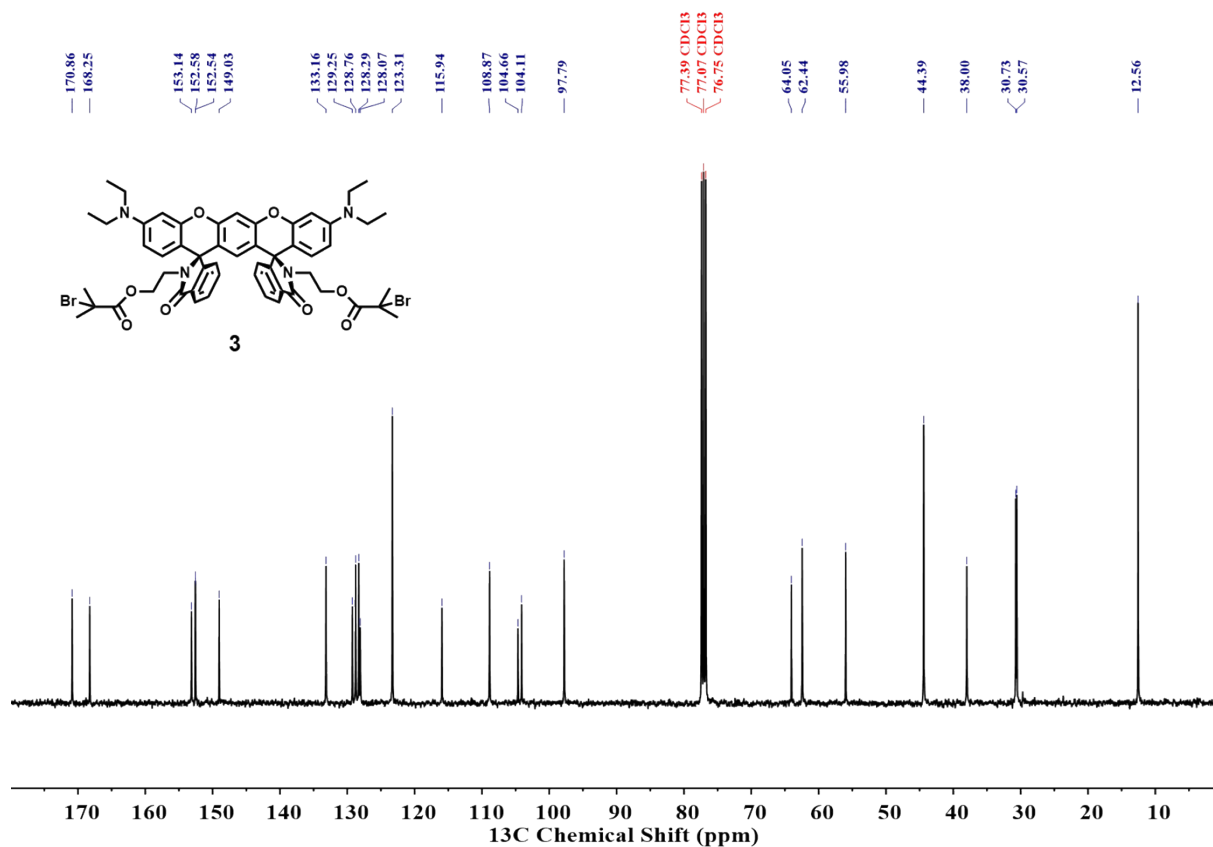
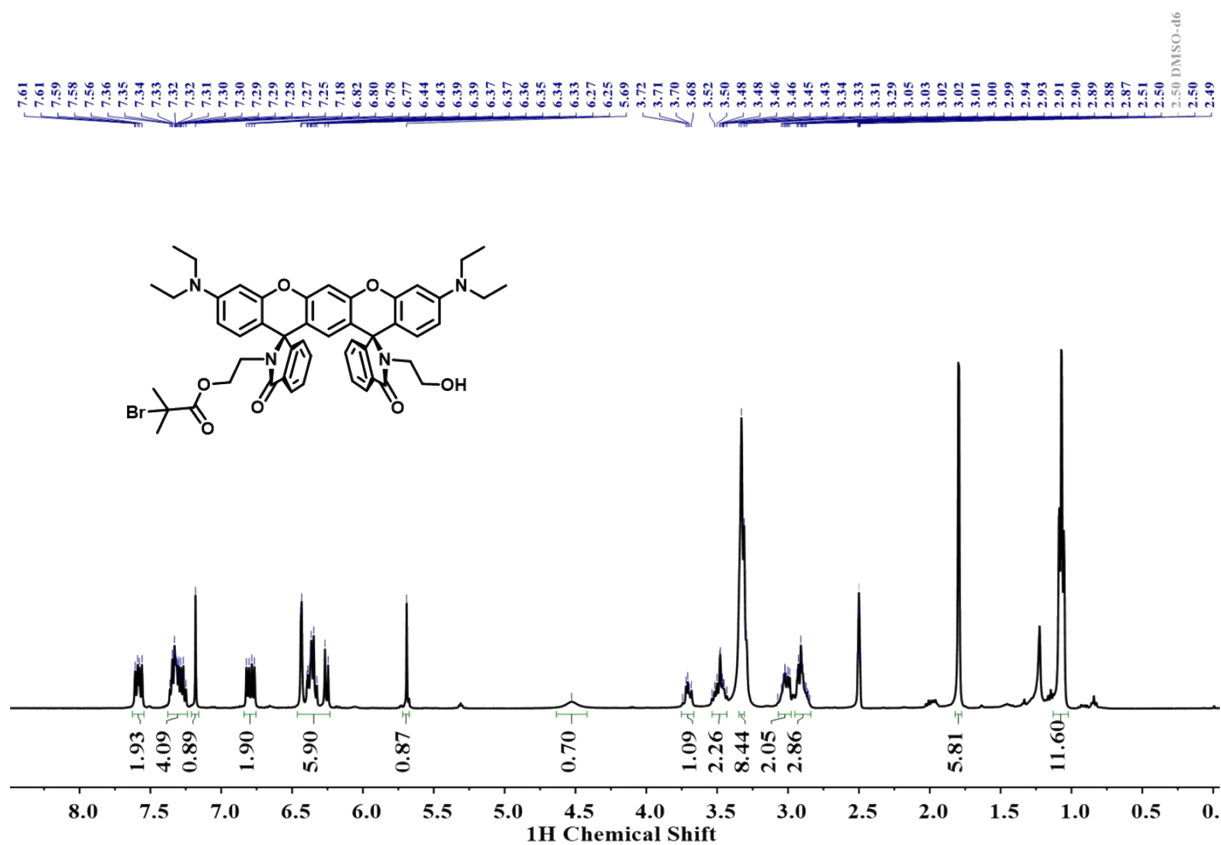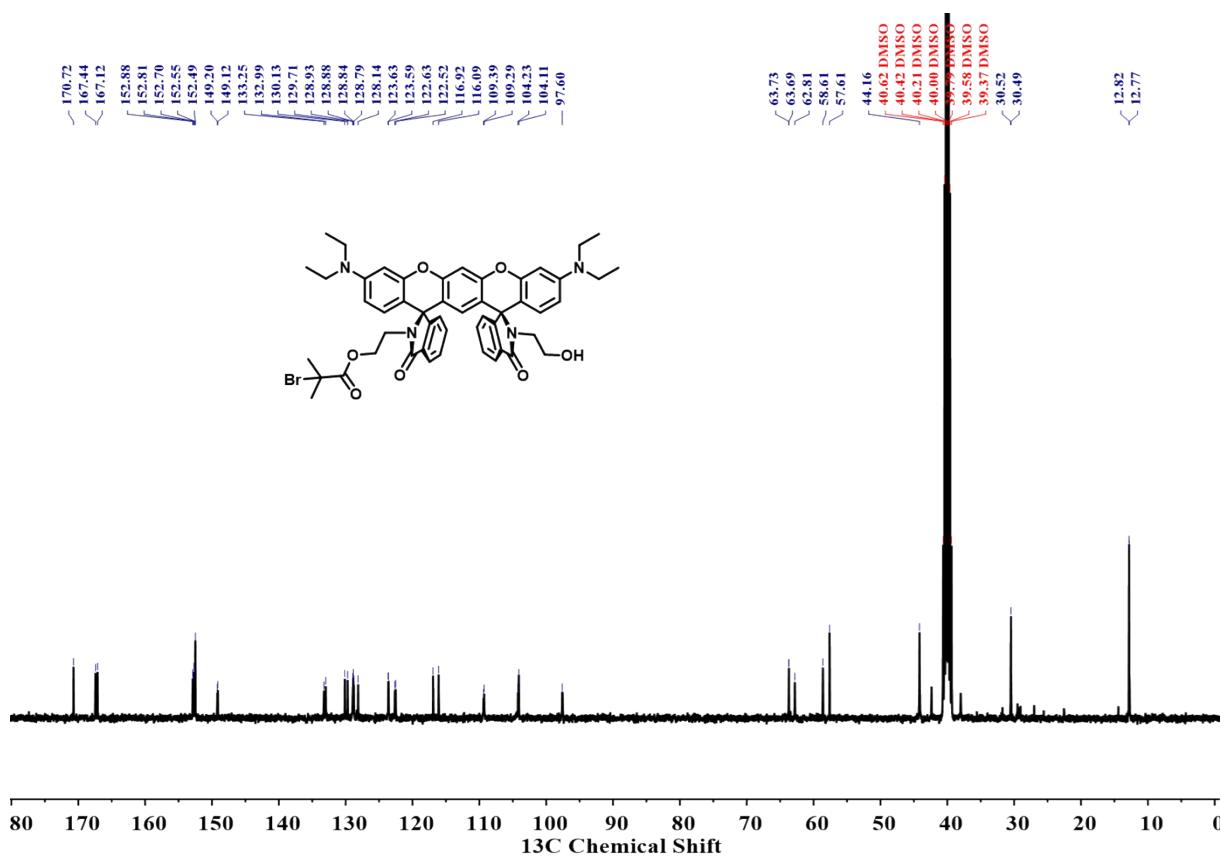Figure S7. ^{13}C NMR spectrum of compound 3 in CDCl$_3$.

Figure S8. ^{1}H NMR spectrum of compound **4** in DMSO-d_6.

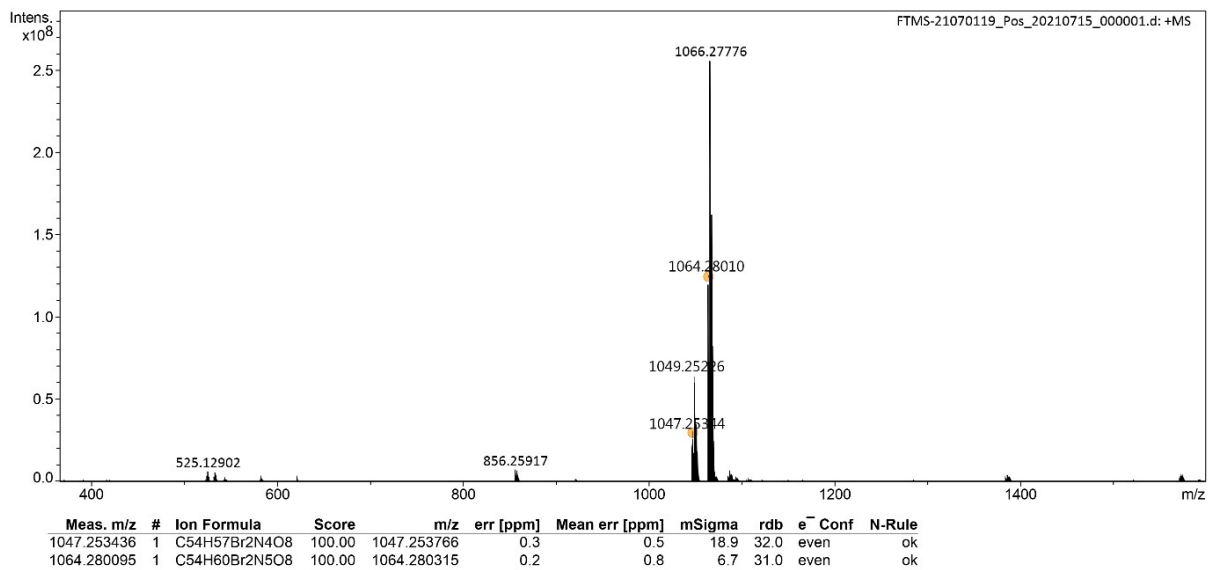Figure S9. ^{13}C NMR spectrum of compound **4** in DMSO-d_6.

Meas. m/z	#	Ion Formula	Score	m/z	err [ppm]	Mean err [ppm]	mSigma	rdb	e⁻ Conf	N-Rule
1047.253436	1	C54H57Br2N4O8	100.00	1047.253766	0.3	0.5	18.9	32.0	even	ok
1064.280095	1	C54H60Br2N5O8	100.00	1064.280315	0.2	0.8	6.7	31.0	even	ok

Figure S10. HR-MS spectrum of compound **3**
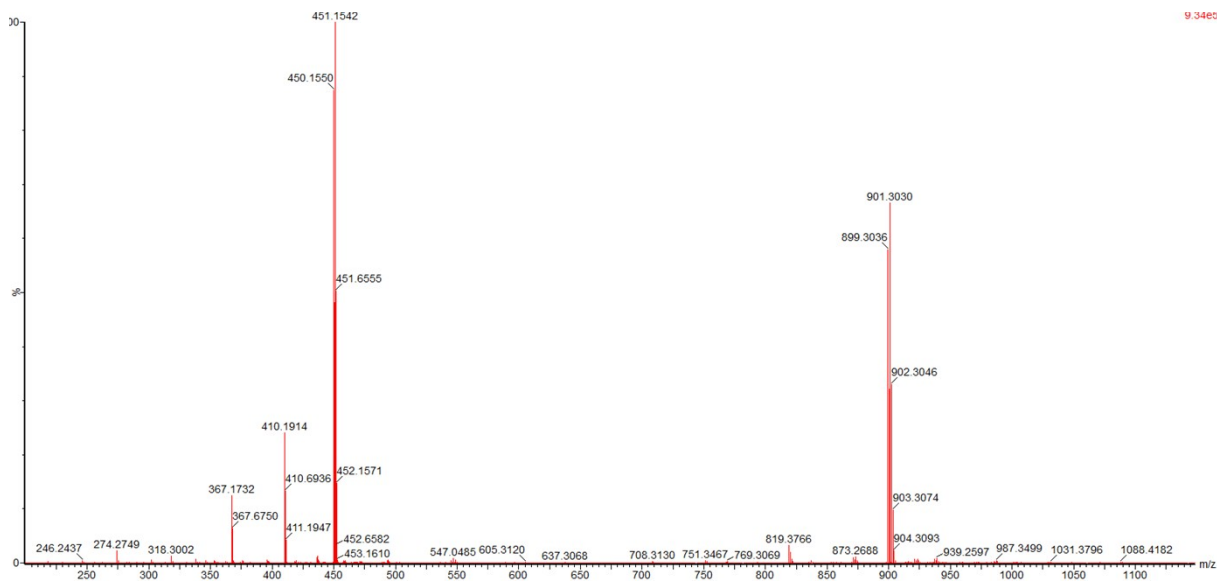
Figure S11. HR-MS spectrum of compound **4**.

ABPX-PMA49
48.6 kDa
$Đ = 1.21$

ABPX-PMA87
86.6 kDa
$Đ = 1.33$

ABPX-PMA130
129.5 kDa
$Đ = 1.51$

ABPX-PMA176
176.2 kDa
$Đ = 1.29$

ABPX-PMA245
245.1 kDa
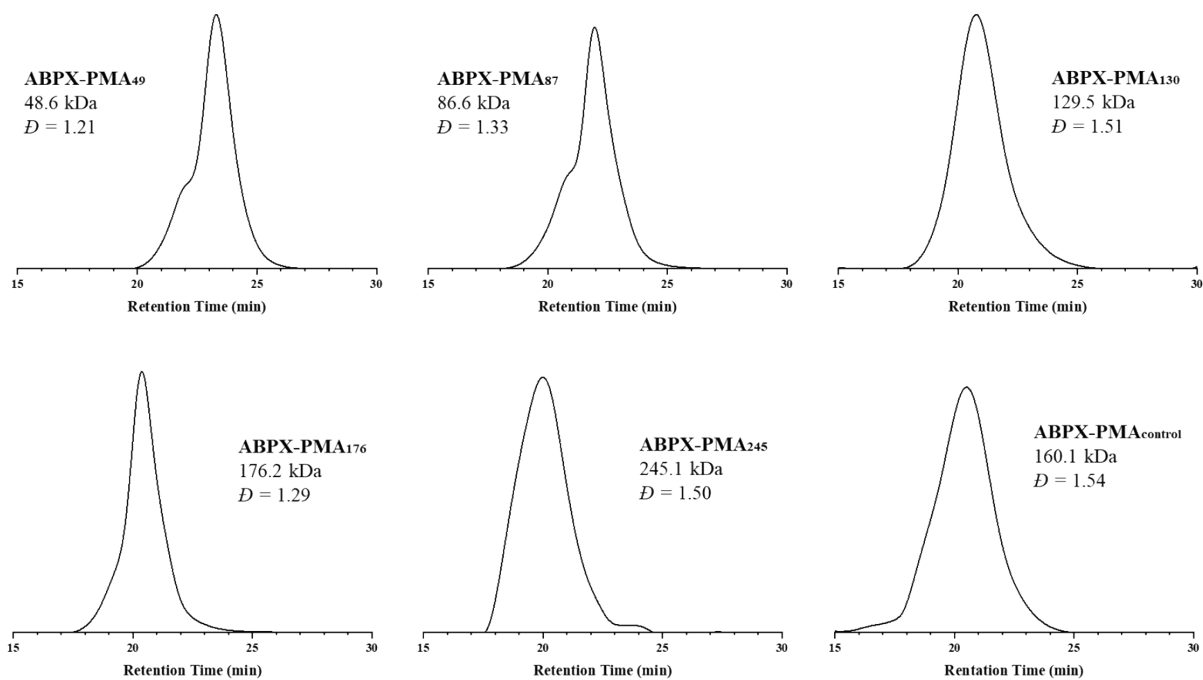$Đ = 1.50$

ABPX-PMAcontrol
160.1 kDa
$Đ = 1.54$

Figure S12. GPC traces (refractive index response), M_n, and dispersity for each polymer.

IV. Supplementary Data Analysis

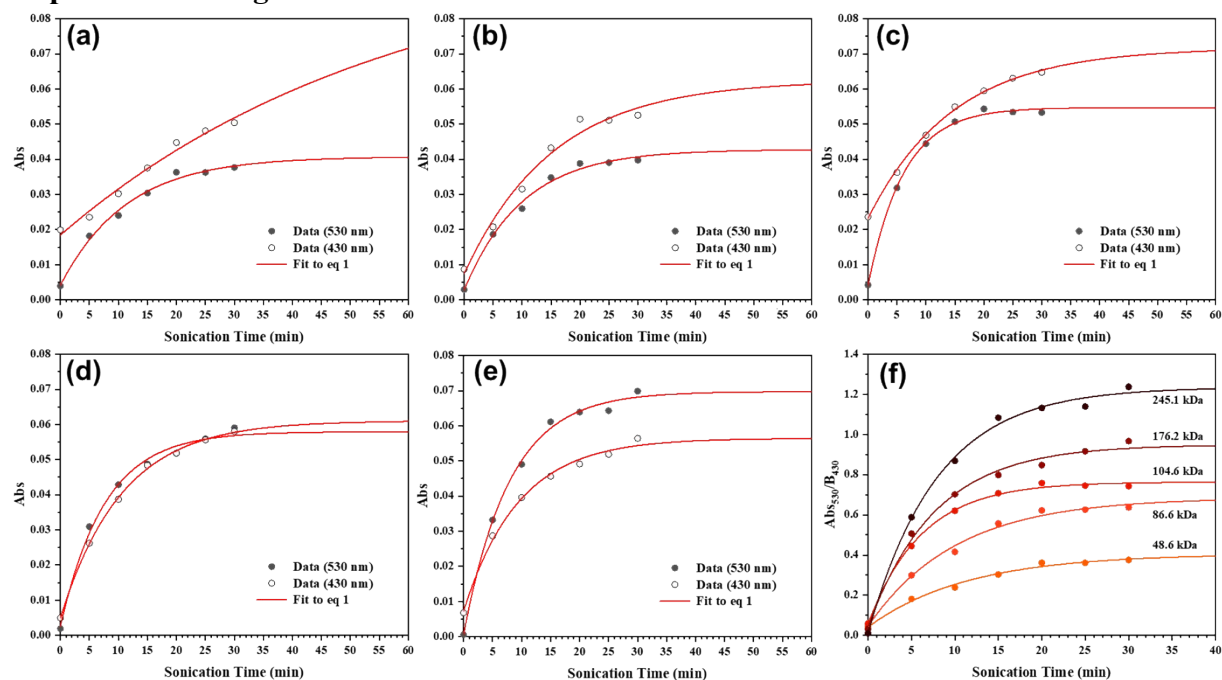## Exponential fitting of absorbance values

Figure S13. Kinetic plots of (a) 48.6 kDa ABPX-PMA$_{49}$, (b) 86.6 kDa ABPX-PMA$_{87}$, (c) 129.5 kDa ABPX-PMA$_{130}$, (d) 176.2 kDa ABPX-PMA$_{176}$, and (e) 245.1 kDa ABPX-PMA$_{245}$. Absorbance at 430 and 530 nm was recorded for each polymer during ultrasound-induced mechanical activation and fitted to eq 1 to calculate B$_{430}$ and B$_{530}$. (f) The absorbance at 530 nm for each polymer was scaled to their respective values of B$_{430}$ and fitted to eq 2.
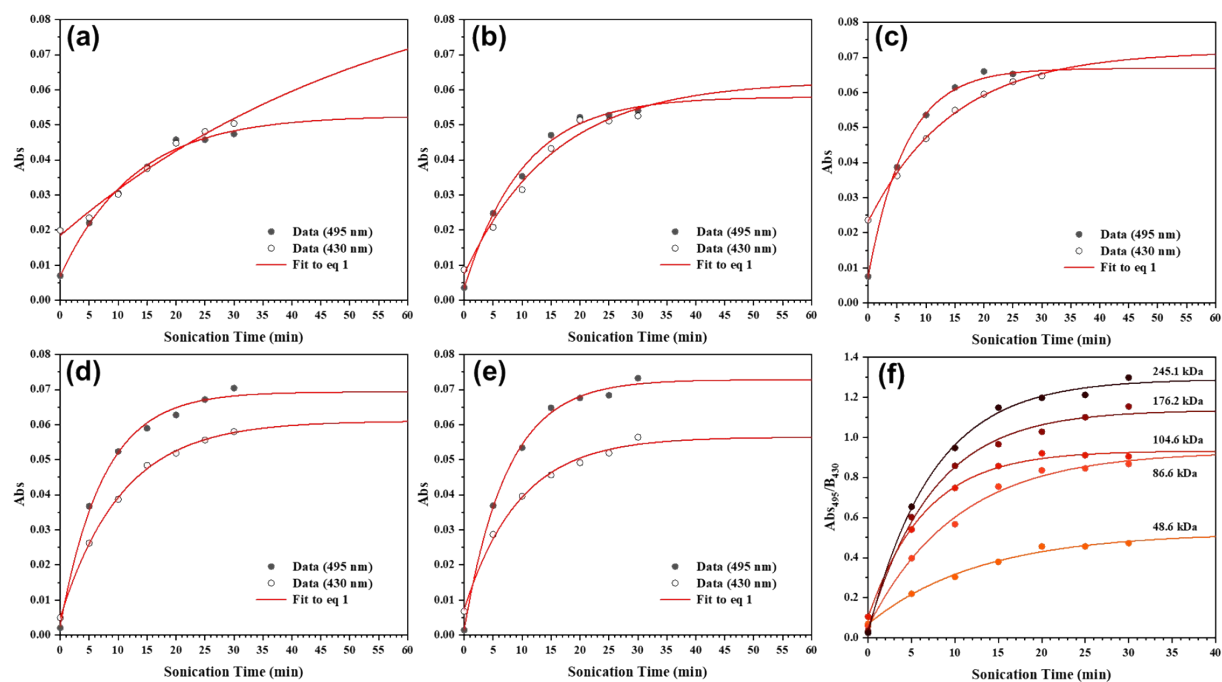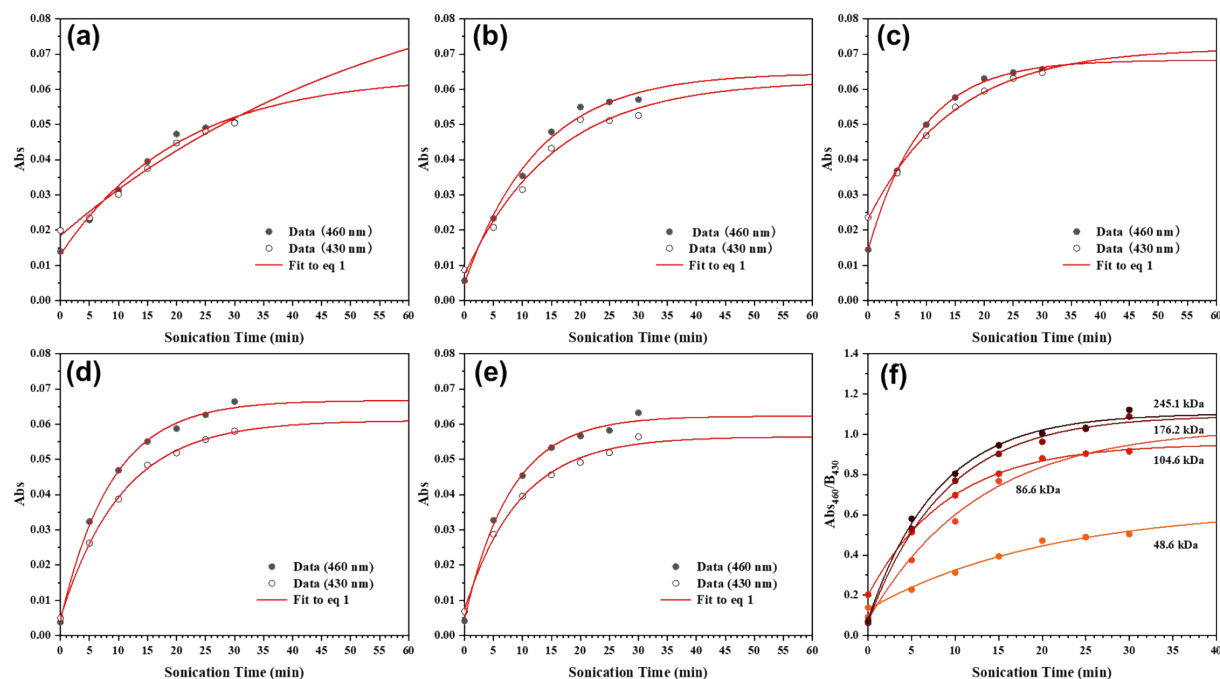

Figure S14. Kinetic plots of (a) 48.6 kDa ABPX-PMA$_{49}$, (b) 86.6 kDa ABPX-PMA$_{87}$, (c) 129.5 kDa ABPX-PMA$_{130}$, (d) 176.2 kDa ABPX-PMA$_{176}$, and (e) 245.1 kDa ABPX-PMA$_{245}$.

Absorbance at 430 and 495 nm was recorded for each polymer during ultrasound-induced mechanical activation and fitted to eq 1 to calculate B_{430} and B_{495}. (f) The absorbance at 495 nm for each polymer was scaled to their respective values of B_{430} and fitted to eq 2.
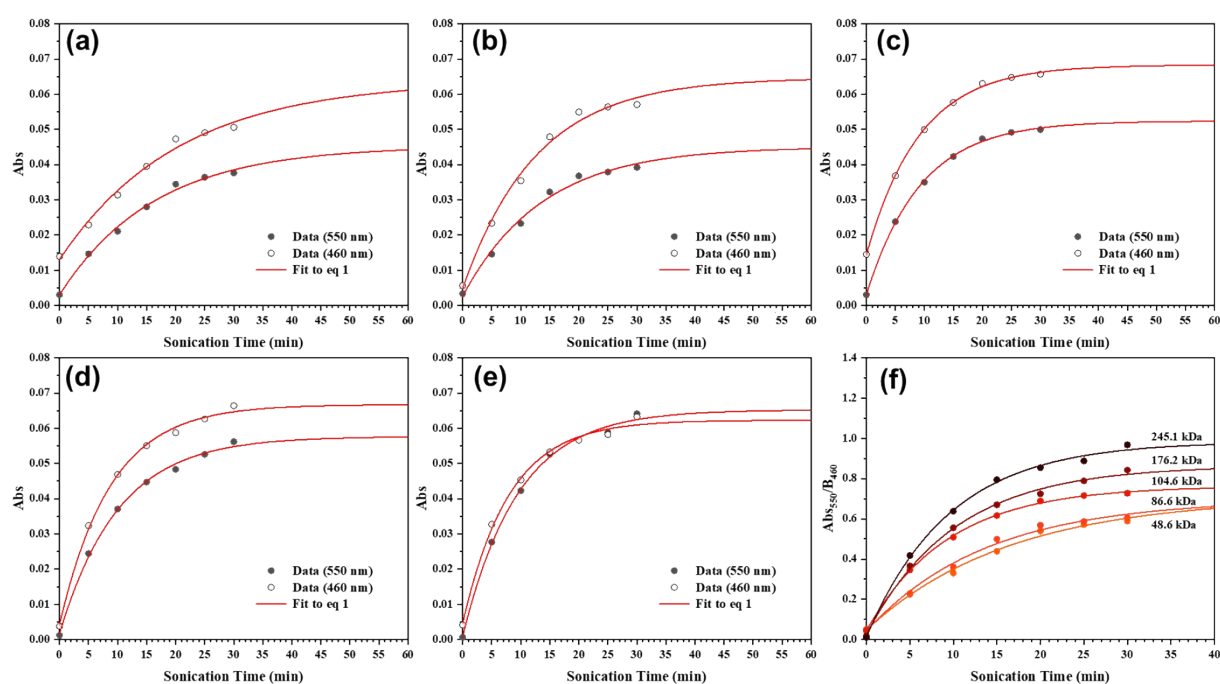

Figure S15. Kinetic plots of (a) 48.6 kDa ABPX-PMA$_{49}$, (b) 86.6 kDa ABPX-PMA$_{87}$, (c) 129.5 kDa ABPX-PMA$_{130}$, (d) 176.2 kDa ABPX-PMA$_{176}$, and (e) 245.1 kDa ABPX-PMA$_{245}$. Absorbance at 430 and 460 nm was recorded for each polymer during ultrasound-induced mechanical activation and fitted to eq 1 to calculate B_{430} and B_{460}. (f) The absorbance at 460 nm for each polymer was scaled to their respective values of B_{430} and fitted to eq 2.

16

Figure S16. Kinetic plots of (a) 48.6 kDa ABPX-PMA$_{49}$, (b) 86.6 kDa ABPX-PMA$_{87}$, (c) 129.5 kDa ABPX-PMA$_{130}$, (d) 176.2 kDa ABPX-PMA$_{176}$, and (e) 245.1 kDa ABPX-PMA$_{245}$. Absorbance at 460 and 550 nm was recorded for each polymer during ultrasound-induced mechanical activation and fitted to eq 1 to calculate B$_{460}$ and B$_{550}$. (f) The absorbance at 550 nm for each polymer was scaled to their respective values of B$_{460}$ and fitted to eq 2.
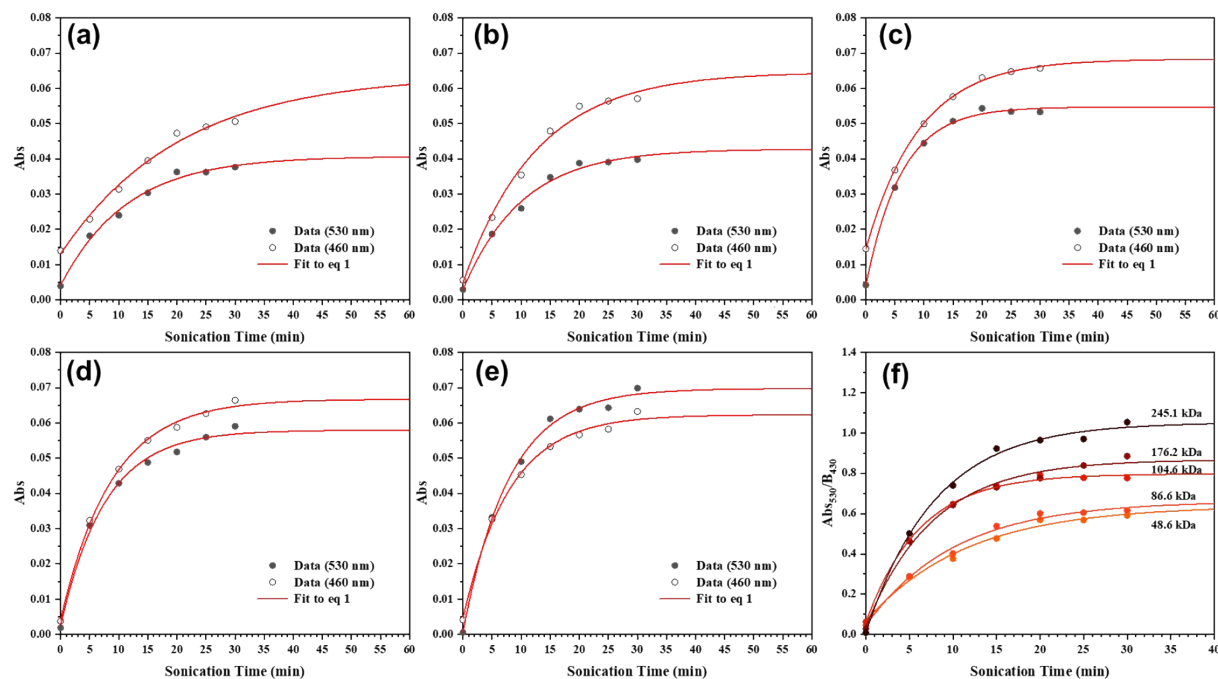

Figure S17. Kinetic plots of (a) 48.6 kDa ABPX-PMA$_{49}$, (b) 86.6 kDa ABPX-PMA$_{87}$, (c) 129.5 kDa ABPX-PMA$_{130}$, (d) 176.2 kDa ABPX-PMA$_{176}$, and (e) 245.1 kDa ABPX-PMA$_{245}$. Absorbance at 460 and 530 nm was recorded for each polymer during ultrasound-induced mechanical activation and fitted to eq 1 to calculate B$_{460}$ and B$_{530}$. (f) The absorbance at 530 nm for each polymer was scaled to their respective values of B$_{460}$ and fitted to eq 2.
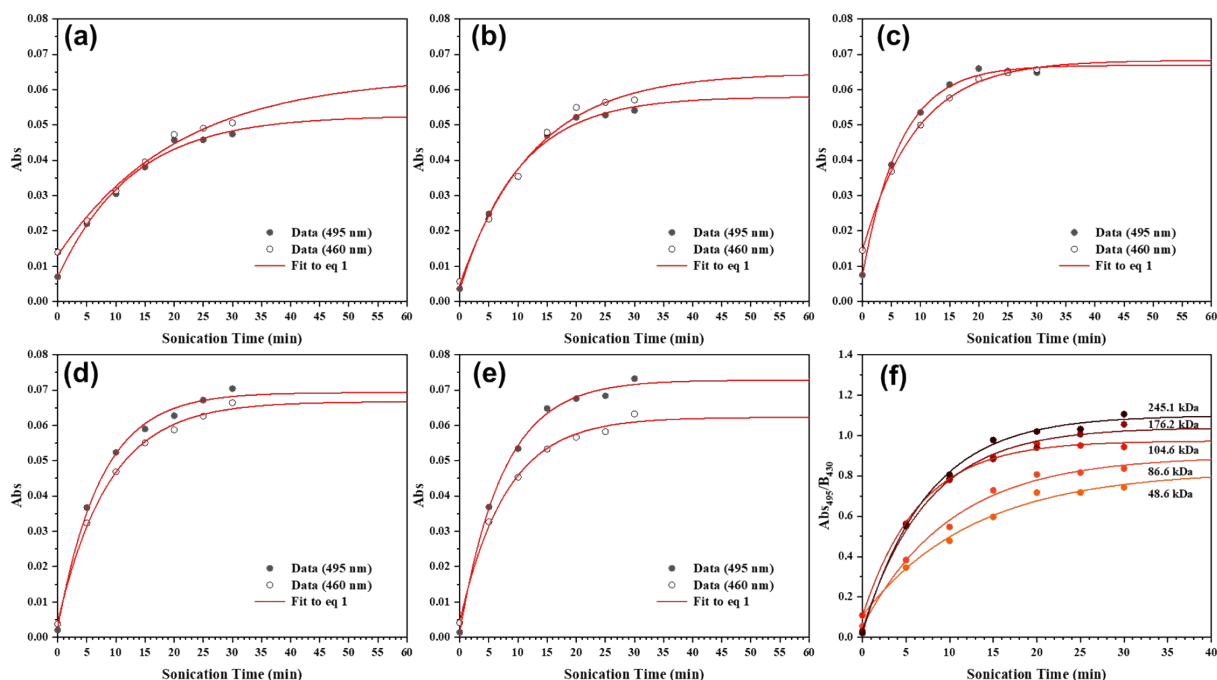
Figure S18. Kinetic plots of (a) 48.6 kDa ABPX-PMA$_{49}$, (b) 86.6 kDa ABPX-PMA$_{87}$, (c) 129.5 kDa ABPX-PMA$_{130}$, (d) 176.2 kDa ABPX-PMA$_{176}$, and (e) 245.1 kDa ABPX-PMA$_{245}$. Absorbance at 460 and 495 nm was recorded for each polymer during ultrasound-induced mechanical activation and fitted to eq 1 to calculate B$_{460}$ and B$_{495}$. (f) The absorbance at 495 nm for each polymer was scaled to their respective values of B$_{460}$ and fitted to eq 2.

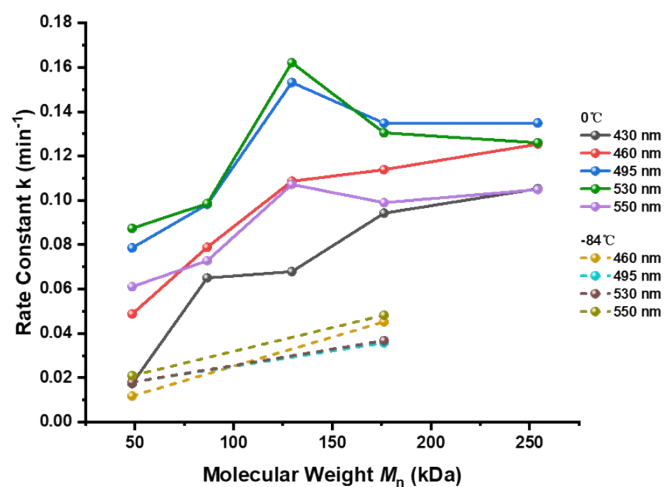| ABPX-PMA (kDa)	0°C					-84°C	
	48.6	86.6	129.5	176.2	245.1	48.6	176.2
k (430 nm, min^{-1})	0.0174	0.0651	0.0679	0.0943	0.1053	-	-
k (460 nm, min^{-1})	0.0488	0.0789	0.1087	0.1139	0.1254	0.0118	0.453
k (495 nm, min^{-1})	0.0786	0.0982	0.1532	0.1348	0.1349	0.0181	0.0368
k (530 nm, min^{-1})	0.0874	0.0986	0.1621	0.1305	0.1260	0.0181	0.0358
k (550 nm, min^{-1})	0.0611	0.0728	0.1072	0.0990	0.1049	0.0210	0.0483

18

Figure S19. Rate constants of all ABPX-PMAs with different M_n sonicated in an ice bath (0°C) or an ethyl acetate bath cooled with liquid nitrogen (-84 °C), which were obtained by fitting the absorption values at 430 nm, 460 nm, 495 nm, 530 nm, and 550 nm.

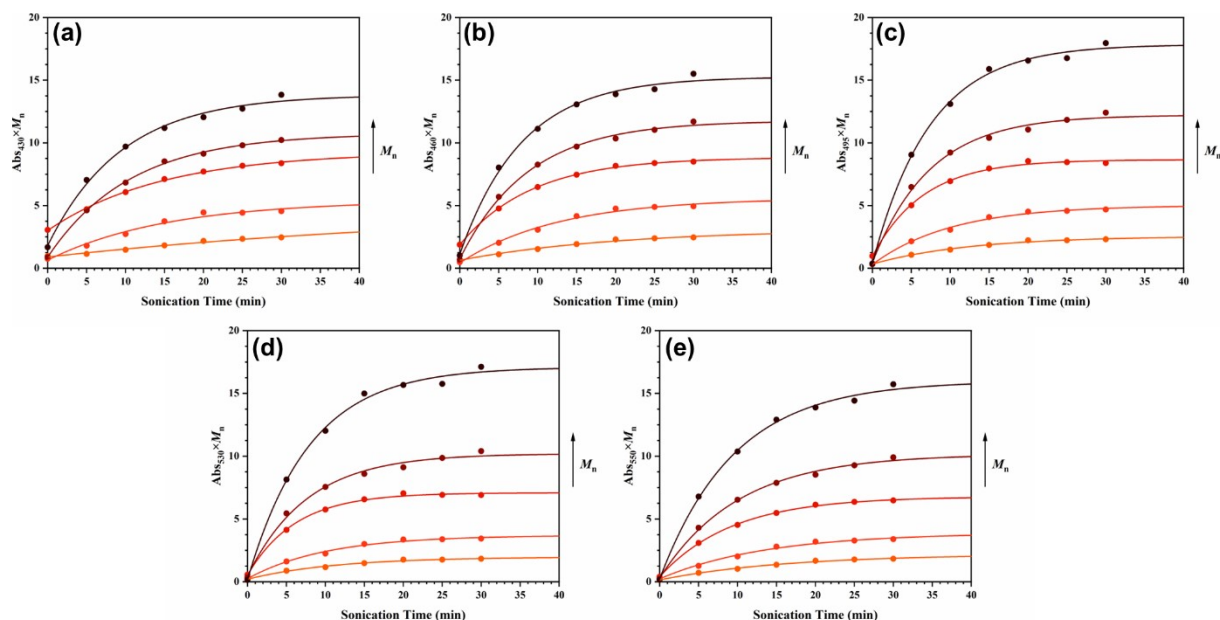**Linear fitting of M$_n$ calibrated equilibrium absorbance values**

Figure S20. M_n-calibrated absorbance at (a) 430 nm, (b) 460nm, (c) 495nm, (d) 530nm, and (e) 550nm for each polymer was fitted to eq 1.
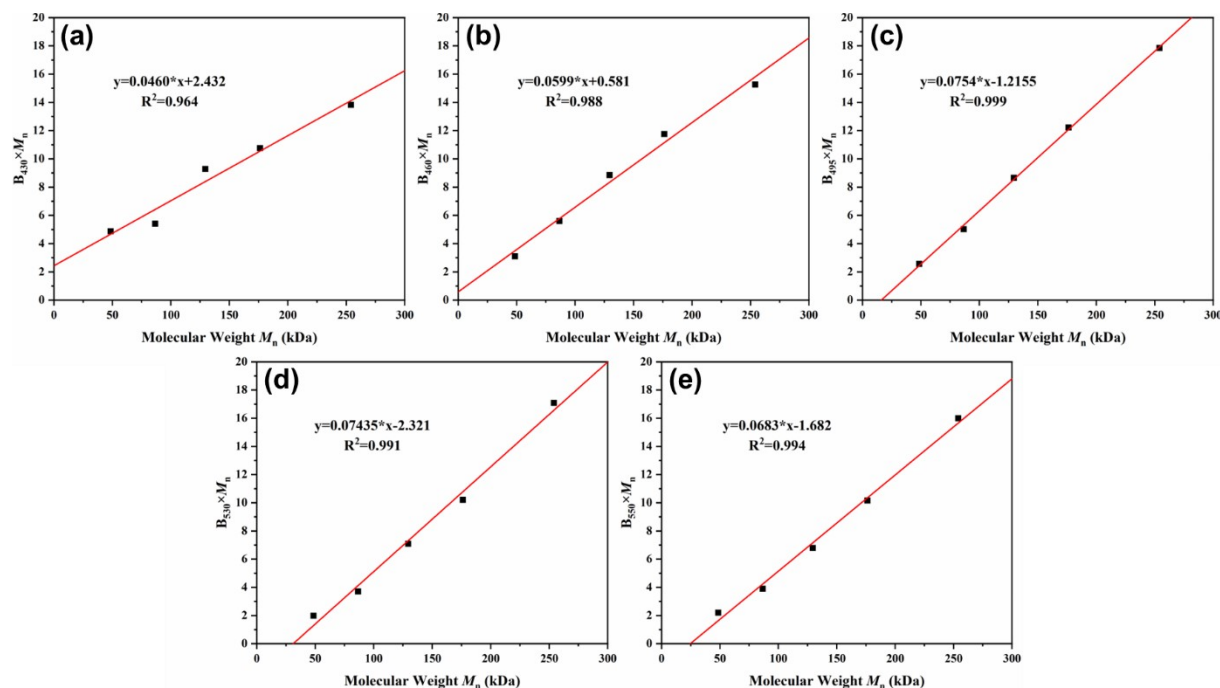

Figure S21. Linear fittings between M_n-calibrated equilibrium absorbance at (a) 430 nm, (b) 460nm, (c) 495nm, (d) 530nm, and (e) 550nm and M_n.
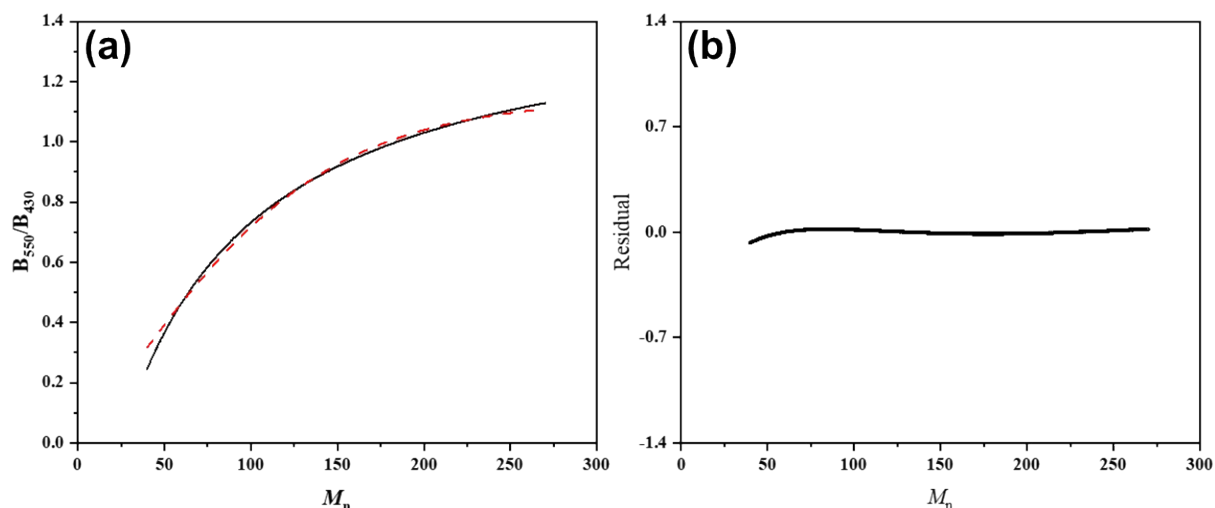
Figure S22. (a) Exponential decay fitting of the eq 3 between 40 kDa ~ 270 kDa. (b) Residual plot. The exponential function was reported by McFadden and Robb, and given by:

$$\frac{B_{550}}{B_{430}} = \left(\frac{\varepsilon_{O-C,430}}{\varepsilon_{O-O,550}} \frac{\left(e^{-c\left(\frac{M_n}{M_0}\right)} \right)}{\left(1 - e^{-c\left(\frac{M_n}{M_0}\right)}\right)} + \frac{\varepsilon_{o-o,430}}{\varepsilon_{o-o,550}} \right) - 1$$

Fitted c was 1.37×10^{-3}, closed to reported value 9×10^{-4}; fitted $\dfrac{\varepsilon_{O-C,430}}{\varepsilon_{O-O,550}}$ and $\dfrac{\varepsilon_{o-o,430}}{\varepsilon_{o-o,550}}$ were 2.03 and 0.87, respectively. The fitted R-square value is 0.996.
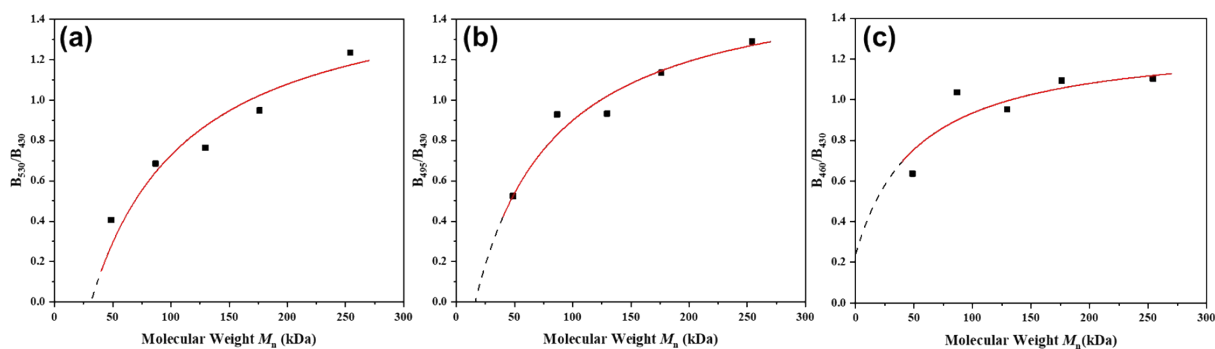
Multimodal analysis

Figure S23. Ratios of (a) B_{530}/B_{430}, (b) B_{495}/B_{430}, and (c) B_{460}/B_{430} determined for polymers of varying M_n. Red solid lines: numerical models derived from linear fittings between M_n-calibrated absorbance and sonication time; black dotted lines: extrapolated numerical models.
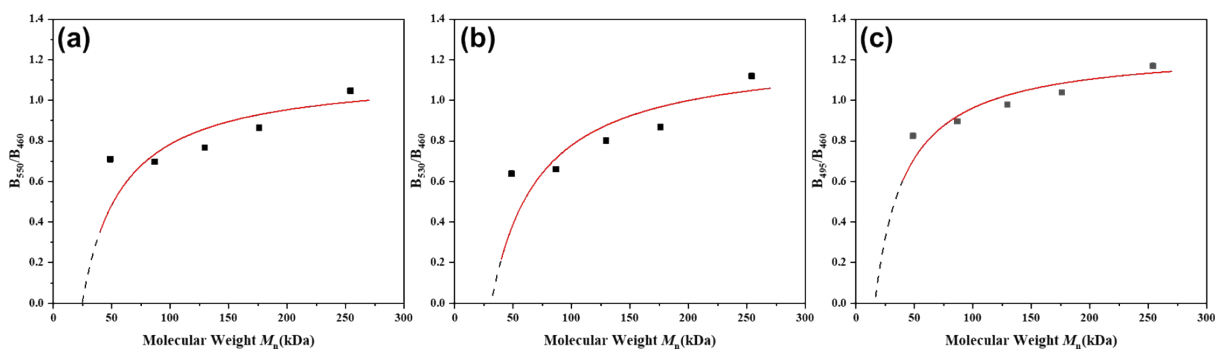

Figure S24. Ratios of (a) B_{550}/B_{460}, (b) B_{530}/B_{460}, and (c) B_{495}/B_{460} determined for polymers of varying M_n. Red solid lines: numerical models derived from linear fittings between M_n-calibrated absorbance and sonication time; black dotted lines: extrapolated numerical models.
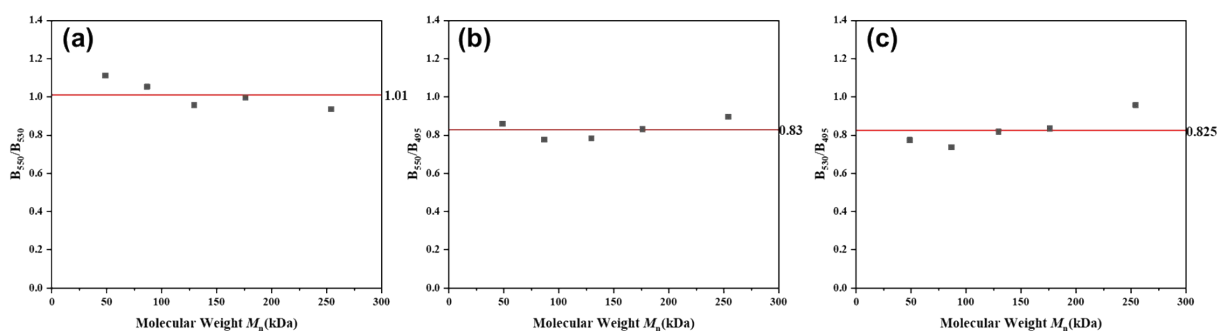

Figure S25. Ratios of (a) B_{550}/B_{530}, (b) B_{550}/B_{495}, and (c) B_{530}/B_{495} determined for polymers of varying M_n. Red solid lines: Data averages.
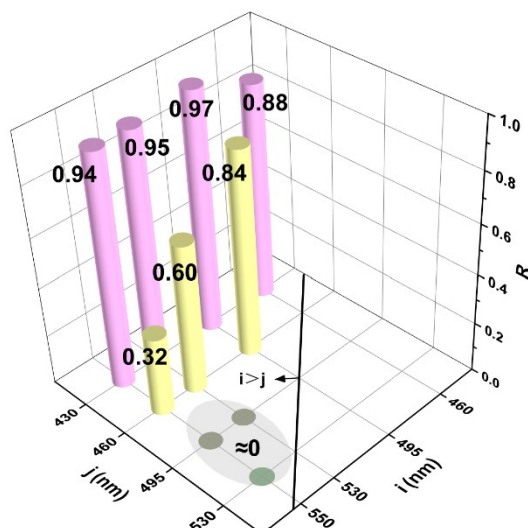
Figure S26. 3D histogram of fitting constants (R) for relevant data in Figure 4c, 5, and S20-22.

We have summarized fitting constants (R) of relevant data as above. We use B_i/B_j (B: steady-state absorption value; i,j: selected two different absorption wavelengths, i>j) to describe the relative distribution of ABPX$_{OO}$ and ABPX$_{OC}$. B_{550}/B_{530}, B_{550}/B_{495}, and B_{530}/B_{495} are almost constant with increasing M_n compared to other (B_i/B_j)s. Thus, ABPX$_{OO}$ predominates at 495 nm, 530 nm, and 550 nm, and we estimate these R≈0. It is clear that the R values are dependent on the choice of ABPX$_{OC}$ characteristic band (j nm) and divided into three parts: 430 nm (high R values 0.88~0.97), 460 nm (moderate R values 0.32~0.84), and 430 nm (low R values ≈0). The moderate R values for B_i/B_{460} (0.32-0.84) and B_{460}/B_{430} (0.88) probably originate from the reported overlapped absorption bands of ABPX$_{OO}$ and ABPX$_{OC}$. It means that the absorption spectra of ABPX$_{OO}$ and ABPX$_{OC}$ overlap less at 430 nm, 495 nm, 530 nm, and 550 nm and more at 460 nm. The eq 2 and B_i/B_j not only describe the relative concentration variation of the double ring-opening product (ABPX$_{OO}$) and the relative distribution of the two ring-opening products, respectively but also assist us in assigning the multiple absorption peaks and achieving the multimodal analysis.

V. Supplementary Experiment

Calibration of solution sonication

The calibration was performed according to the very recent work,[2] A small Dewar was filled with 200 mL of water and the probe was submerged approximately 2 cm into the water. The exact height was marked and used throughout all ultrasound experiments. A thermocouple was then introduced into the water and the temperature was allowed to stabilize. The amplitude on the Lawson Scientific DH92-IIN ultrasonic generator was set to 20%, the initial temperature was recorded, and sonication was started. The temperature of the water was recorded every 20 s for 3 min, and these values were plotted against time to determine $\Delta T / \Delta t$ by the slope of the line (Figure S21a). This procedure was repeated for amplitudes of 30, 40, 60, and 80%. The heat due to cavitation was calculated by: $Q = \Delta C_p(H_2O) \cdot m(H2O) \cdot \Delta T/\Delta t$, where $\Delta C_p(H_2O) = 4.179$ J g^{-1} K^{-1}, m(H2O) = 200 g. The resulting heat Q was divided by the surface area of the horn tip (0.785 cm^2 for a 10 mm diameter horn) to obtain the power intensity of ultrasound in W cm^{-2}. Finally, the power intensity was plotted against the percentage of amplitude to generate the calibration curve (Figure S21b). The output power during sonication was estimated to be 12.12 W cm^{-2}.
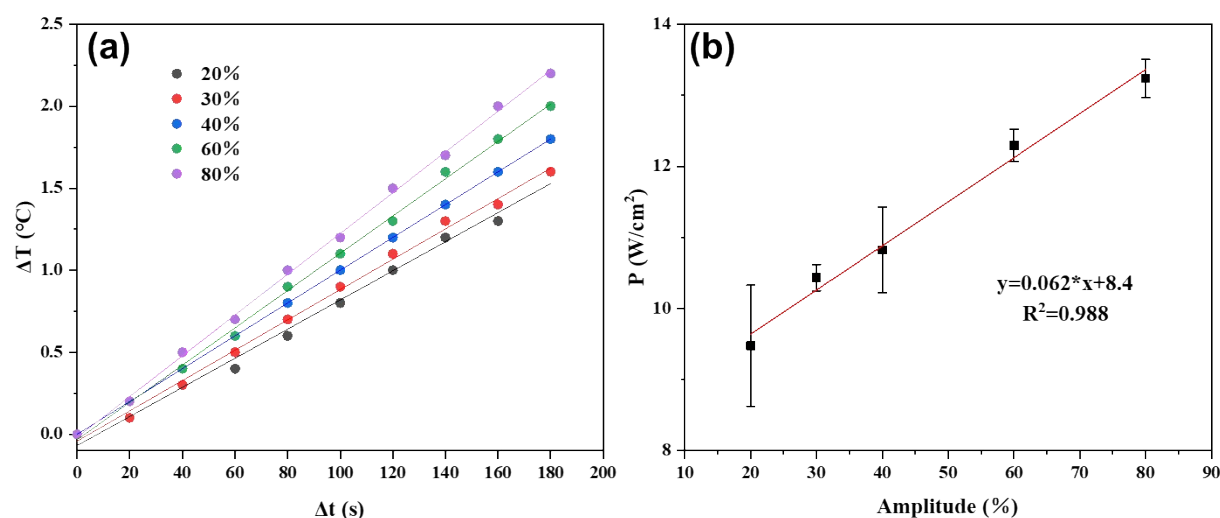

Figure S27. (a) Time-temperature curves measured during sonication under different applied amplitudes. (b) The calibration curve obtained by linear fitting between the heat due to cavitation, and the amplitude. Error bars are derived from three parallel experiments.
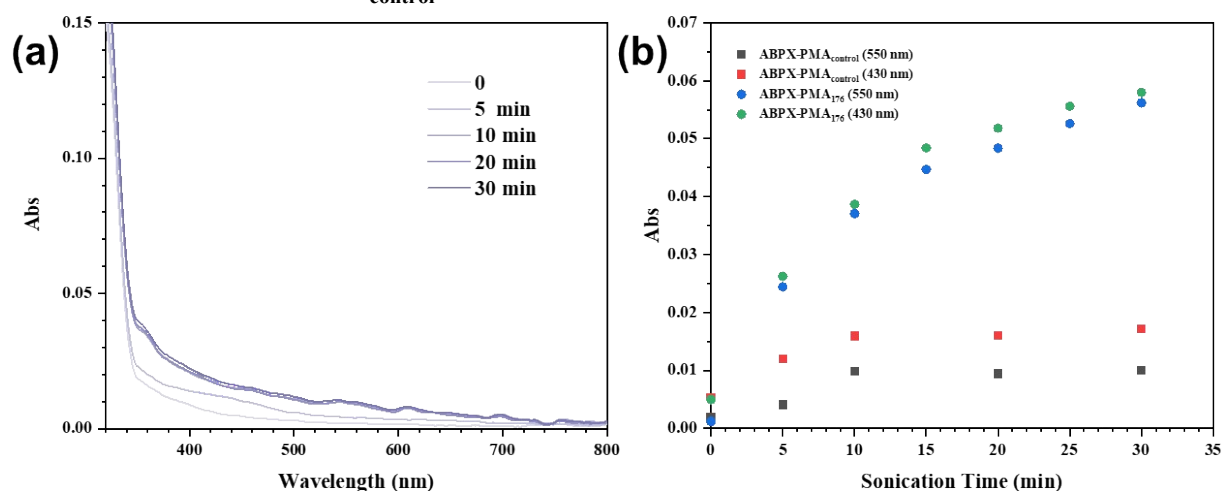
Sonication of ABPX-PMA_control

Figure S28. (a) UV−vis absorption curves of 160.1 kDa ABPX-PMA_control subjected to ultrasound-induced mechanochemical activation. (b) Absorbance monitored at 550 nm and 430 nm during sonication of ABPX-PMA_control and ABPX-PMA_176.
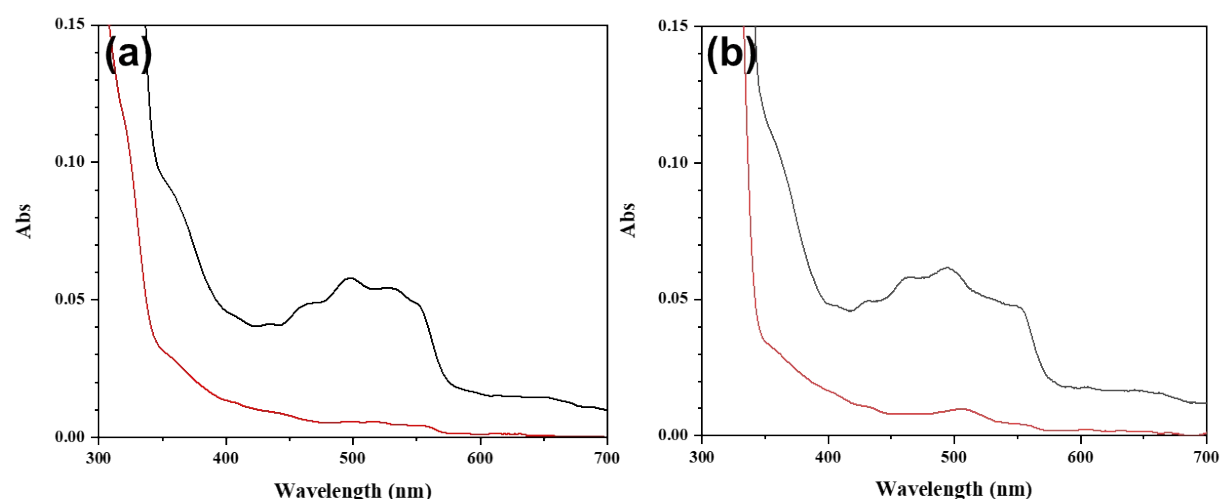
Thermal recovery

Figure S29. UV-vis absorption curves before and after thermal recovery of (a) 245.1 kDa ABPX-PMA_245, and (b) 176.2 kDa ABPX-PMA_176. Black lines: UV-vis absorption curves after 30 min sonication; red lines: UV-vis absorption curves after a week at room temperature.
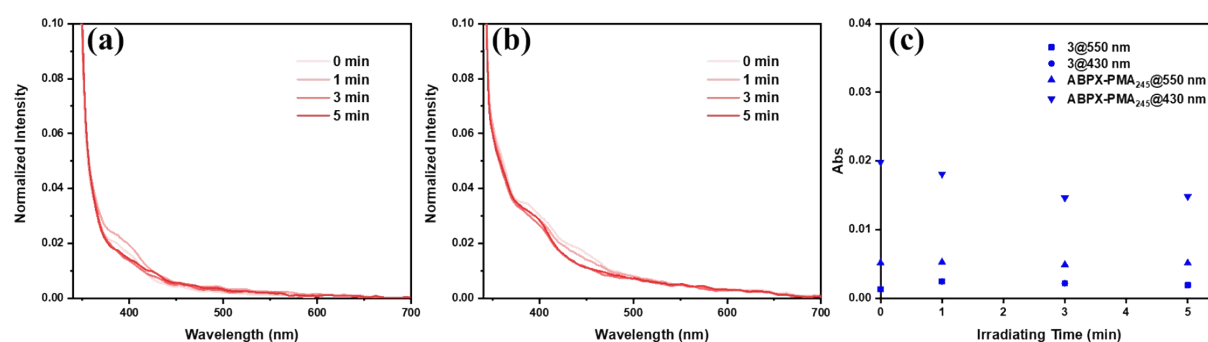
Photoresponse of ABPX initiator 3 and ABPX-PMA

Figure S30. UV−vis absorption curves of (a) ABPX initiator 3 and (b) ABPX-PMA$_{245}$ in THF irradiated by 365 nm UV light. (b) Absorbance monitored at 550 nm and 430 nm during irradiating by 365 nm UV light for ABPX initiator 3 and ABPX-PMA$_{245}$ in THF.

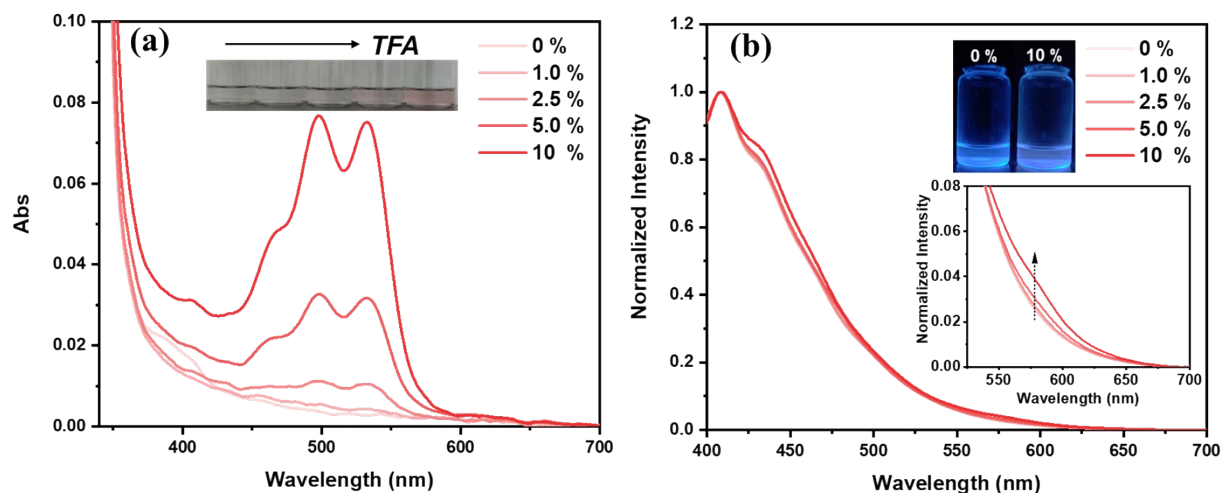**Acidichromism of ABPX initiator 3**

Figure S31. Absorption (a) and fluorescence emission (b) spectra of 3 in various combinations of trifluoroacetic acid (TFA) and THF (1 mM). The inserts in (a) and (b) show the color changes before and after adding TFA under day light and 365 nm UV light, respectively.
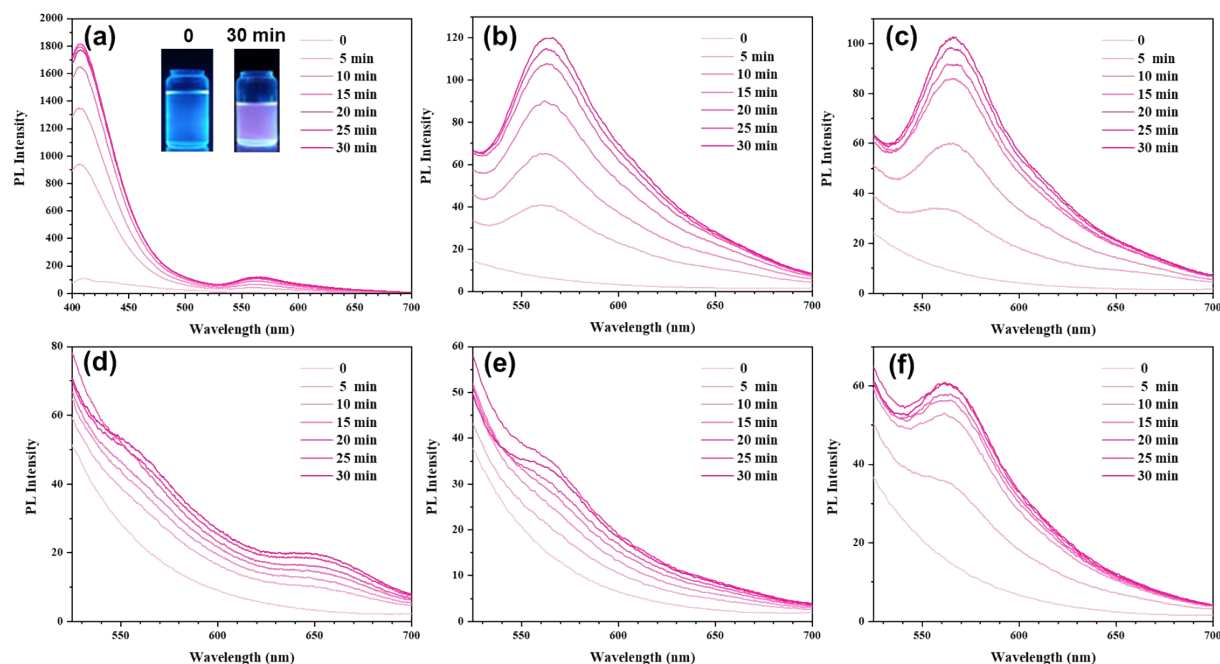
Fluorescence spectra

Figure S32. (a) Representative fluorescence spectra in the wavelength range 400−700 nm of ABPX-PMA$_{245}$ subjected to ultrasound-induced mechanochemical activation for varying amounts of time. Insert left: initial fluorescence image; insert right: fluorescence image after 30

min sonication. The strong fluorescence peaks between 400-450 nm after sonication are attributed to the ring-opening products, corresponding to the apparent increase of absorption between 340 nm to 400 nm (Figure 1), which is also observed in absorption spectra of acidochromism.[3] Fluorescence curves were scaled to the wavelength range 525−700 nm for (b) 245.1 kDa ABPX-PMA$_{245}$, (c) 176.2 kDa ABPX-PMA$_{176}$, (d) 129.5 kDa ABPX-PMA$_{130}$, (e) 86.6 kDa ABPX-PMA$_{87}$, and (f) 48.6 kDa ABPX-PMA$_{49}$.

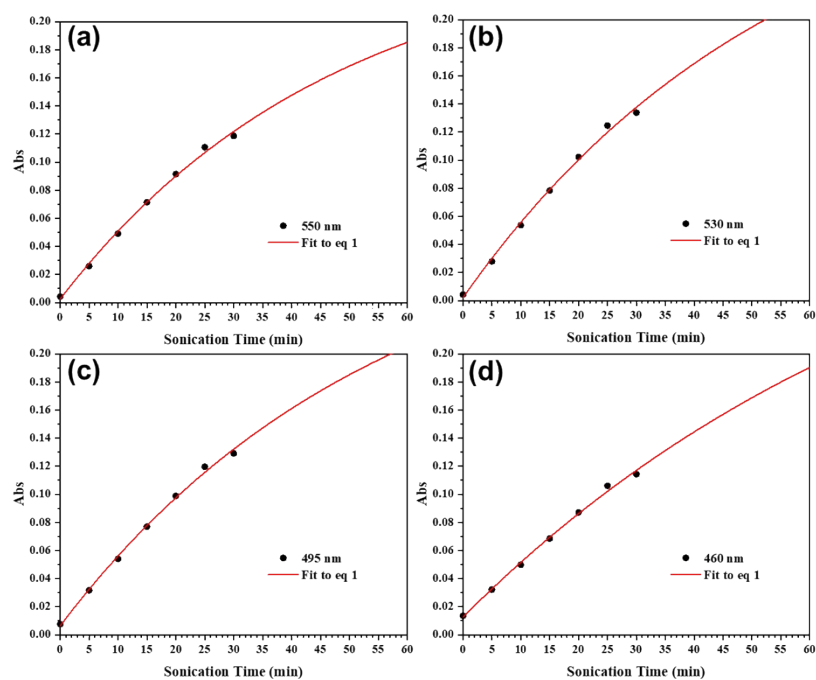**Sonication under an ethyl acetate bath cooled with liquid nitrogen**

Figure S33. Kinetic plots of 48.6 kDa ABPX-PMA$_{49}$ at (a) 550 nm, (b) 530 nm (c) 495 nm, and (d) 460 nm.
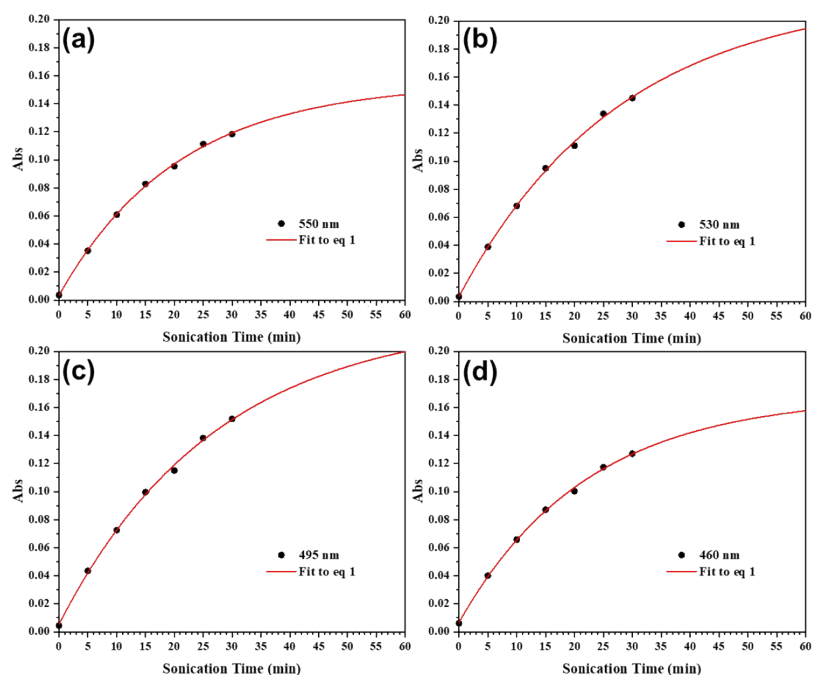
Figure S34. Kinetic plots of 176.2 kDa ABPX-PMA$_{176}$ at (a) 550 nm, (b) 530 nm (c) 495 nm, and (d) 460 nm.

VI. DFT Calculations (CoGEF)

CoGEF calculations of ABPX (*cis* and *trans* forms) were performed using Gaussian 16[4] according to previously reported methods. Ground state energies were calculated using DFT at the B3LYP/6-31G* level of theory. The equilibrium conformations of the unconstrained molecules were initially calculated followed by optimization of the equilibrium geometries. Starting from the equilibrium geometry of the unconstrained molecules (energy = 0 kJ/mol), the distance between the terminal methyl groups of the truncated structures was increased in increments of 1 Å or 0.02 Å (near the break of the C-C bond) and the energy was minimized at each step.
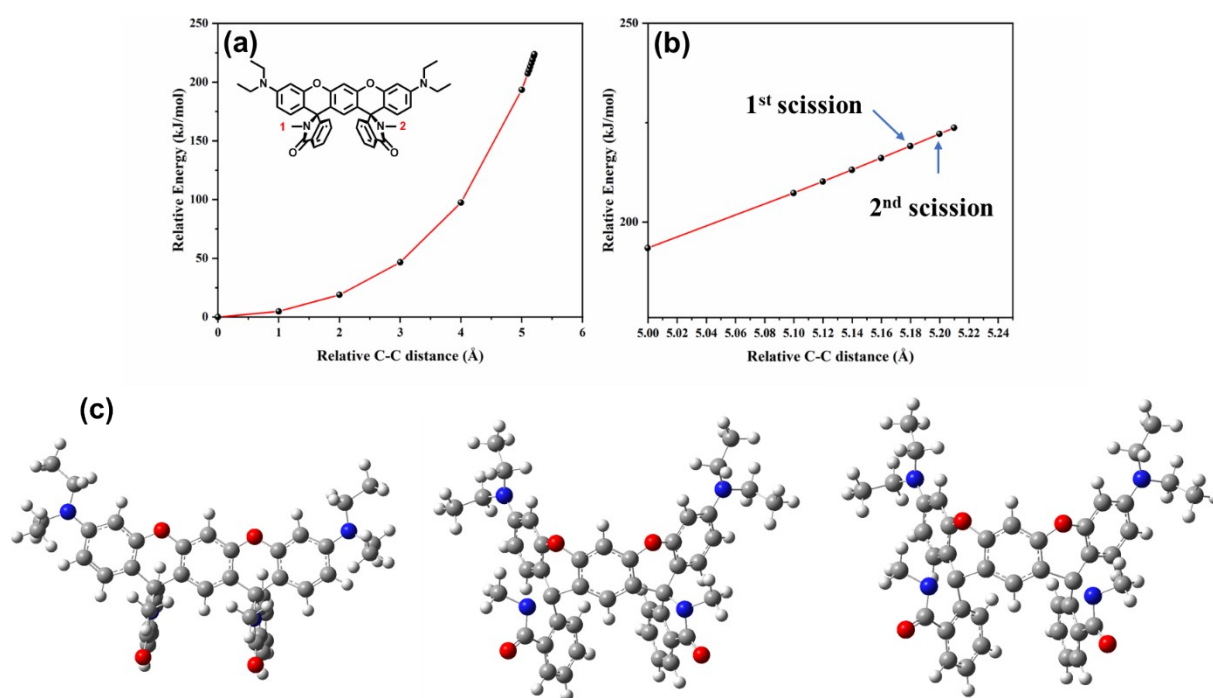

Figure S35. (a) and (b) Energy-displacement diagram under external force field for *cis* ABPX. The arrows indicate the two ring-opening reactions. (c) The corresponding computed structures of the truncated molecules (insert in Figure a). Left: unconstrained ABPX form; middle: ABPX$_{OC}$ form; right: ABPX$_{OO}$ form.
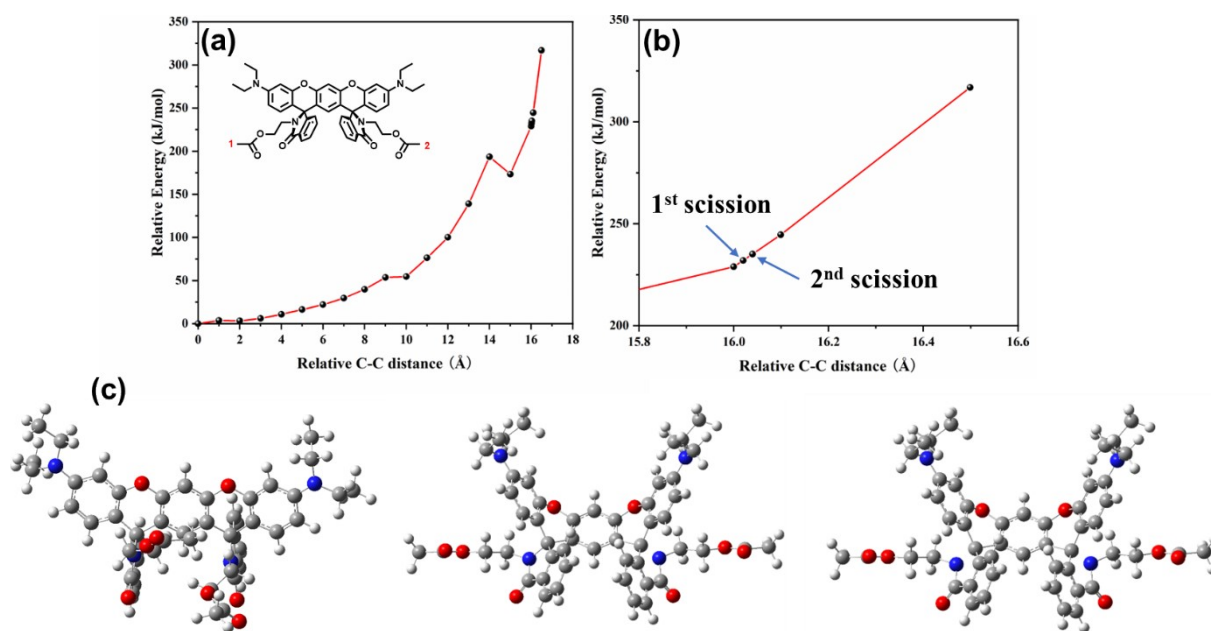
Figure S36. (a) and (b) Energy-displacement diagram under external force field for *cis* ABPX with tethers. The arrows indicate the two ring-opening reactions. (c) The corresponding computed structures of the truncated molecules (insert in Figure a). Left: unconstrained ABPX form; middle: ABPX$_{OC}$ form; right: ABPX$_{OO}$ form.
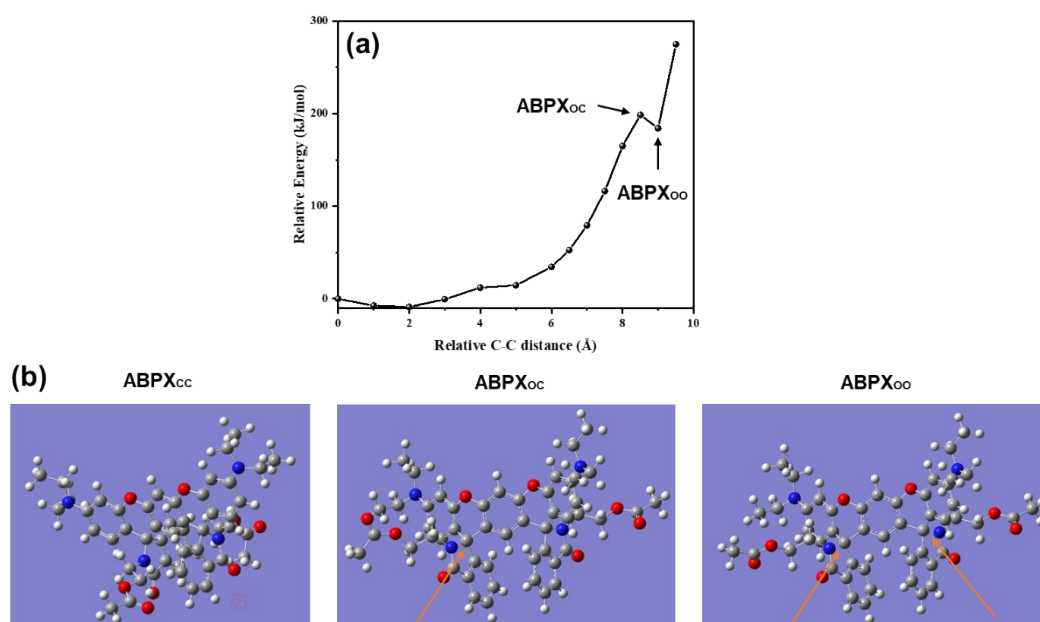

Figure S37. (a) Energy-displacement diagram under external force field for *trans* ABPX with tethers. The arrows indicate the two ring-opening products. (b) The corresponding computed structures of *trans* ABPX. Left: unconstrained ABPX form; middle: ABPX$_{OC}$ form; right: ABPX$_{OO}$ form. The relative shorter change of C-C distance between ABPX$_{CC}$ and ABPX$_{OC/CC}$

compared with *cis* ABPX is originated from the pristine longer C-C distance of *trans* ABPX (11.76 Å versus 4.24 Å). The energy decrease from $ABPX_{OC}$ to $ABPX_{OO}$ is attributed to the flip of the side chain ester groups.
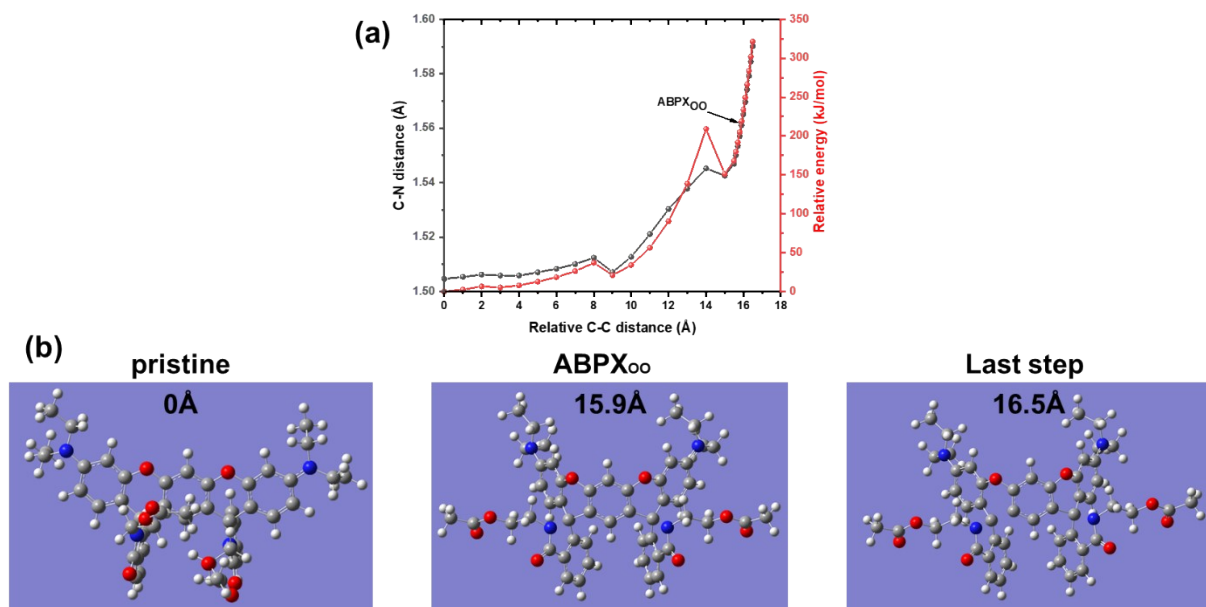

Figure S38. (a) Energy-displacement and C-N distance-displacement profiles under external force field for the truncated structure with tethers using PCM (dielectric constant is 37). (b) The corresponding computed structures of *cis* ABPX.
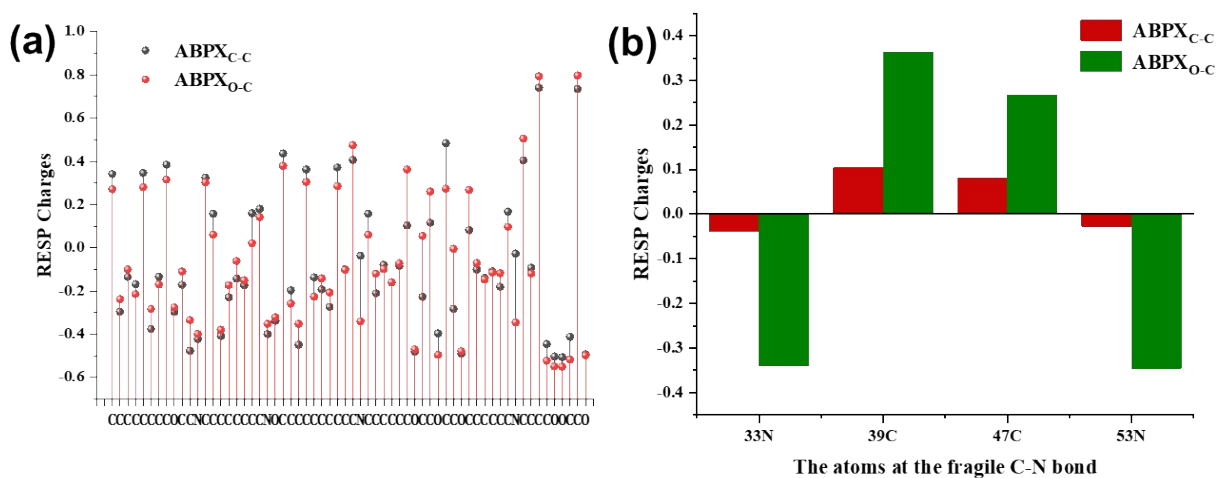

Figure S39. Computed RESP charges[5] of $ABPX_{OC}$ and $ABPX_{OO}$ (*cis* form) using Multiwfn software for (a) the whole molecule and (b) the atoms at the fragile C-N bond. Atoms are numbered by Gaussian software.
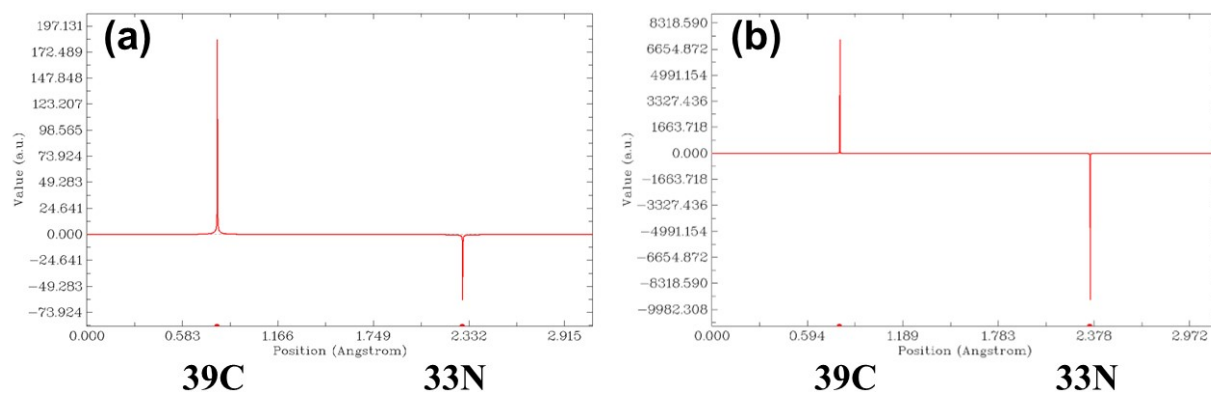
Figure S40. Computed electrostatic potential at the broken C-N bond in ABPX$_{OC}$ for (a) ABPX$_{CC}$ and (b) ABPX$_{OC}$ (*cis* form) using Multiwfn software. Atoms are numbered by Gaussian software.

VII.   References

[1] Y. Shirasaki, S. Kamino, M. Tanioka, K. Watanabe, Y. Takeuchi, S. Komeda and S. Enomoto, *Chem. - Asian J.*, 2013, **8**, 2609-2613.

[2] Y. Liu, S. Holm, J. Meisner, Y. Jia, Q. Wu, T. J. Woods, T. J. Martinez, J. S. Moore, *Science* 2021, **373**, 208.

[3] S. Kamino, A. Muranaka, M. Murakami, A. Tatsumi, N. Nagaoka, Y. Shirasaki, K. Watanabe, K. Yoshida, J. Horigome, S. Komeda, M. Uchiyama and S. Enomoto, *Phys. Chem. Chem. Phys.*, 2013, **15**, 2131-2140.

[4] Gaussian 16, Revision A.03, M. J. Frisch, G. W. Trucks, H. B. Schlegel, G. E. Scuseria, M. A. Robb, J. R. Cheeseman, G. Scalmani, V. Barone, G. A. Petersson, H. Nakatsuji, X. Li, M. Caricato, A. V. Marenich, J. Bloino, B. G. Janesko, R. Gomperts, B. Mennucci, H. P. Hratchian, J. V. Ortiz, A. F. Izmaylov, J. L. Sonnenberg, D. Williams-Young, F. Ding, F. Lipparini, F. Egidi, J. Goings, B. Peng, A. Petrone, T. Henderson, D. Ranasinghe, V. G. Zakrzewski, J. Gao, N. Rega, G. Zheng, W. Liang, M. Hada, M. Ehara, K. Toyota, R. Fukuda, J. Hasegawa, M. Ishida, T. Nakajima, Y. Honda, O. Kitao, H. Nakai, T. Vreven, K. Throssell, J. A. Montgomery, Jr., J. E. Peralta, F. Ogliaro, M. J. Bearpark, J. J. Heyd, E. N. Brothers, K. N. Kudin, V. N. Staroverov, T. A. Keith, R. Kobayashi, J. Normand, K. Raghavachari, A. P. Rendell, J. C. Burant, S. S. Iyengar, J. Tomasi, M. Cossi, J. M. Millam, M. Klene, C. Adamo, R. Cammi, J. W. Ochterski, R. L. Martin, K. Morokuma, O. Farkas, J. B. Foresman, and D. J. Fox, Gaussian, Inc., Wallingford CT, 2016.

[5] C. I. Bayly, P. Cieplak, W. Cornell, P. A. Kollman, *J. Chem. Phys.* 1993, **97**, 10269-10280.